Electrochemical Surface Area Quantification, CO2 Reduction Performance, and Stability Studies of Unsupported Three-Dimensional Au Aerogels versus Carbon-Supported Au Nanoparticles

Journal Article

Author(s):
Chauhan, Piyush; Hiekel, Karl; Diercks, Justus S.; Herranz, Juan; Saveleva, Viktoriia A.; Khavlyuk, Pavel; Eychmüller, Alexander; Schmidt, Thomas ⓘD

Article

Electrochemical Surface Area Quantification, CO₂ Reduction Performance, and Stability Studies of Unsupported Three-Dimensional Au Aerogels versus Carbon-Supported Au Nanoparticles

Piyush Chauhan, Karl Hiekel, Justus S. Diercks, Juan Herranz,* Viktoriia A. Saveleva, Pavel Khavlyuk, Alexander Eychmüller, and Thomas J. Schmidt

Read Online

ACCESS | 📊 Metrics & More | 📄 Article Recommendations | 🔲 Supporting Information

ABSTRACT: The efficient scale-up of CO₂-reduction technologies is a pivotal step to facilitate intermittent energy storage and for closing the carbon cycle. However, there is a need to minimize the occurrence of undesirable side reactions like H₂ evolution and achieve selective production of value-added CO₂-reduction products (CO and HCOO⁻) at as-high-as-possible current densities. Employing novel electrocatalysts such as unsupported metal aerogels, which possess a highly porous three-dimensional nanostructure, offers a plausible approach to realize this. In this study, we first quantify the electrochemical surface area of an Au aerogel (≈5 nm in web thickness) using the surface oxide-reduction and copper underpotential deposition methods. Subsequently, the aerogel is tested for its CO₂-reduction performance in an in-house developed, two-compartment electrochemical cell. For comparison purposes, similar measurements are also performed on polycrystalline Au and a commercial catalyst consisting of Au nanoparticles supported on carbon black (Au/C). The Au aerogel exhibits a faradaic efficiency of ≈97% for CO production at ≈−0.48 V_{RHE}, with a suppression of H₂ production compared to Au/C that we ascribe to its larger Au-particle size. Finally, identical-location transmission electron microscopy of both nanomaterials before and after CO₂-reduction reveals that, unlike Au/C, the aerogel network retains its nanoarchitecture at the potential of peak CO production.

KEYWORDS: electrocatalyst, copper underpotential deposition, identical-location transmission electron microscopy, hydrogen evolution reaction, particle size effect
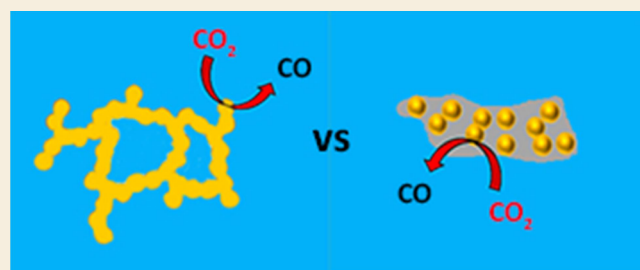
INTRODUCTION

The electrochemical reduction of CO₂ is increasingly considered a promising approach to tackle ongoing challenges in energy conversion while helping to reduce the emissions of CO₂ resulting from anthropogenic activities.[1−4] In particular, the conversion of this CO₂ into carbon-based fuels and value-added chemicals using energy from renewable sources like solar or wind can effectively take a step toward closing the carbon-based energy cycle. In addition, the sustainable production of chemical fuels and feedstock materials is advantageous, as it is compatible with the existing infrastructures for transportation and industrial applications, and it could serve to buffer the intermittent nature of renewable energy production technologies.[5]

While the CO₂-reduction reaction (CO₂RR) can lead to a variety of products (e.g., CO, CH₄, C₂H₄, HCOO⁻, and CH₃OH), only formate (HCOO⁻) or carbon monoxide (CO) has been found to be economically viable when compared to established, industrial production pathways.[6] In this regard, Au-based catalysts (including alloys, like Au$_x$Cu$_y$) have been

reported to display the highest selectivity for the production of CO.[7,8] The seminal experiments by Hori and co-workers, dating back as early as the 1980s, were the first to show a CO faradaic efficiency (FE) of up to 92% at −0.98 V versus the normal hydrogen electrode (V_{NHE}) and ≈2.2 mA·cm$_{geo}$⁻² using polycrystalline Au.[9] Based on these and subsequent results on polycrystalline and single-crystal model surfaces,[10−13] in recent years the research focus has shifted toward Au-based nanostructured electrocatalysts whose increased surface areas allow reaching the high CO-specific current densities needed for device implementation.[14−19] In doing so, numerous studies have tackled the effect of such Au-nanoparticles' size and shape
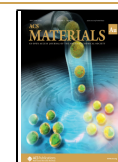
(and corresponding surface faceting) on the CO_2RR-selectivity.

In electrocatalysis, such relations are customarily inferred by comparing the surface-specific activity (SSA) of a series of catalysts with different particle sizes and/or shapes and corresponding electrochemical surface areas (ECSAs),[20−23] whereby the SSA values correspond to the samples' ECSA-normalized currents at a potential at which their performance is (mostly) determined by the reaction kinetics. In the CO_2-electrocatalysis field, however, studies often fail to perform an accurate assessment of the ECSAs of the involved nanomaterials and/or to utilize this crucial metric to normalize the CO_2RR-current density,[24] additionally hindering the comparison of their results with resembling studies. As an example of this, Mistry and co-workers[14] evaluated the surface area of size-selected Au-nanoparticles approximated to spheres and supported on quasi-planar $SiO_2/Si(111)$ wafers based on their height and number in atomic force microscopy measurements but performed the corresponding CO_2-reduction experiments on equivalent nanoparticles coated on glassy carbon substrates with a far-from-planar surface (i.e., a roughness factor (RF) of ≈ 10 $cm_{surface}^2 \cdot cm_{geom}^{-2}$),[25,26] thus putting into question the reliability of their surface-area-normalized current densities. On the other hand, Mascaretti et al.[15] derived their ECSAs from double-layer capacitance measurements known to yield inaccurate values because of the significant deviations in specific double-layer capacitances among porous catalysts, which can be aggravated by an erroneous choice of potential windows and/or scan rates.[27,28] Alternatively, other studies have determined the ECSA of Au electrocatalysts using metal underpotential deposition (UPD) methods based on the potential-controlled adsorption of a (sub)monolayer of Pb or Cu on the Au surface, in what probably constitutes the most reliable technique to this end.[29−32] However, these measurements were systematically performed in a potentiodynamic manner (i.e., recording cyclic voltammograms (CVs) at a given potential scan rate), whereby the slow kinetics of such UPD processes and inaccuracies in the choice of the cathodic inversion potential can lead to significant imprecisions in the inferred ECSA values.[16,17] Therefore, there is a clear need for defining good practices for ECSA evaluation that should allow an unambiguous comparison of the CO_2-reduction performance of the different Au-based electrocatalysts found in the literature.

Beyond these considerations, the use of nanostructured catalysts is often combined with that of carbon supports that improve the nanoparticles' dispersion and concomitantly increase the catalysts' ECSA, but it can also shift the product selectivity toward undesirable H_2 because of the intrinsic H_2-evolution activity of C-surfaces.[33−36] This could be possibly circumvented by employing unsupported catalysts, among which aerogels consisting of a three-dimensional (3D) network of interconnected nanowires feature high porosity and large surface areas[37] required for their implementation in device-applicable electrodes. More specifically, noble metal aerogels present an exciting prospect in the field of electrocatalysis, because they combine the high catalytic activity and excellent charge transfer properties of noble metals[38] with an unsupported nature that can be beneficial to the materials' stability.[39−41] Despite being studied for more than a decade, only a few reports involving electrochemical applications of noble metal aerogels exist, including studies showing their utilization as catalysts for oxygen evolution, oxygen reduction,

or ethanol oxidation,[42−44] with only a few studies having analyzed these materials' potential for CO_2-electroreduction.[45]

With these considerations, this work presents a systematic electrochemical study of an unsupported Au aerogel (Au_{AG}) as a CO_2-reduction electrocatalyst—a first, to the best of our knowledge. To put the results obtained with this Au aerogel into perspective, we employ two other Au-based materials as performance benchmarks, namely, polycrystalline gold (Au_{PC}) and a commercial catalyst consisting of Au-nanoparticles supported on carbon black (Au/C). We first conduct detailed electrochemical characterization of these three Au-based electrocatalysts to determine their ECSAs on the basis of the surface oxide-reduction charge and of the copper under-potential deposition (Cu-UPD) method in a rotating disk electrode (RDE) setup. This is complemented by identical-location transmission electron microscopy (IL-TEM) measurements of the same nanomaterials, with which we verify their possible degradation during electrochemical conditioning. Finally, we test the CO_2 electroreduction performance of Au_{AG}, Au/C, and Au_{PC} in an in-house developed electrochemical cell implementing online gas chromatography for product quantification,[46] and compare the CO_2RR performance of these materials with previous literature data for Au-nanocatalysts. This is complemented by additional (post-mortem) IL-TEM measurements of the Au_{AG} and Au/C catalysts that are used to assess the changes in their nanostructure following CO_2-electroreduction. In this study, we show that Cu-UPD performed with potential holds provides a much more reliable way of estimating ECSAs as compared to using potential-sweeps for Cu-UPD. Additionally, it is revealed that Au_{AG} shows superior selectivity for CO production and higher structural stability during CO_2-reduction as compared to Au/C.

■ EXPERIMENTAL SECTION

Synthesis of Au Aerogels

The synthesis route of the 3D Au aerogel is analogous to the literature.[47] First, 0.1 mmol $HAuCl_4 \cdot 3H_2O$ (>99.9% trace metal basis, Sigma-Aldrich) was dissolved in 492 mL of water. Next, 3 mL of 0.143 M $NaBH_4$ (>96%, Sigma-Aldrich) was quickly added, and the whole solution was stirred for 30 min. Afterward, the solution is split into two equal parts, and 100 mL of toluene (p.a.) was added to each part and vigorously shaken manually for 30 s. The gel pieces were collected at the phase boundary, and subsequently, an acetone exchange was performed. Finally, the gel was transferred to an autoclave (13200J0AB, SPI Supplies) for a solvent exchange to liquid CO_2 and later supercritical drying (37 °C and 90 bar).

Chemicals and Gases for the Electrochemical Measurements

The electrolytes employed in the ECSA and CO_2-reduction measurements were prepared from 96% H_2SO_4 (Suprapur, Merck) and $KHCO_3$ (99.95% trace metals basis, Sigma-Aldrich), respectively. The Cu-UPD experiments were performed using $CuSO_4 \cdot 5H_2O$ (99.999% trace metal basis, Sigma-Aldrich) and NaCl (≥ 99.999%, TraceSELECT, Fluka). All electrolytes were prepared in the specified concentrations by diluting these salts in the required volumes of ultrapure water (18.2 MΩ·cm, ELGA Purelab Ultra). High-purity N_2 and CO_2 (6.0 vs 5.5 grades, respectively—Messer Schweiz AG) were bubbled through the electrolytes to saturate them with the respective gases.

Electrochemical Methods for ECSA Quantification

The electrochemical measurements for estimating the ECSAs in acidic media were performed in the RDE configuration in a custom glass cell (Schmizo AG). A gas bubbler facilitated direct bubbling of N_2 into the

electrolyte before the experimental run for 1 h to remove the dissolved O_2 from the electrolyte. Later, the gas bubbler allowed N_2 blanketing during the experimental procedure. A gold-mesh (Advent Research Materials) fixed with a PTFE-stopper and a K_2SO_4-saturated Hg/HgSO$_4$ electrode (RE-2CP, ALS Co. Ltd.) served as the counter and reference electrodes, respectively. The reference electrode was precalibrated versus the reversible hydrogen electrode (RHE) scale in the same electrolyte saturated with H_2 by performing H_2 evolution/oxidation measurements on a polycrystalline Pt RDE, and hence the potentials mentioned in the ECSA part of this study are expressed as V_{RHE}. The reference electrode was placed inside an electrolyte-filled glass tube with its lower end tapering into a fluorinated ethylene-propylene tube (FEP, Zeus Industrial Products Inc.) plugged with a porous glass frit (Ametek G0300) in contact with the electrolyte.

Three Au-based catalysts were employed as working electrodes during the ECSA study: a polycrystalline Au disk (Pine Research Instrumentation), a 20 wt % Au on Vulcan XC-72 carbon black commercial catalyst (Premetek Co.), and the Au aerogel for which the synthesis is described above. The 5 mm diameter Au$_{PC}$ and glassy carbon disks (HTW Hochtemperatur-Werkstoffe) used to immobilize the powder samples underwent mechanical polishing with 3, 1, and 0.25 μm diamond suspensions (Electron Microscopy Sciences) on a micropolishing cloth (Bühler) in decreasing size order, as to attain a mirror-like finish. After polishing, the disks were sonicated in isopropyl alcohol (99%, VWR) and ultrapure water twice for 5 min each. Following this step, the disks were mounted on an interchangeable rotating ring-disk electrode (RRDE, Pine Research Instrumentation) with a PTFE shroud and an Au ring that did not serve as an active electrode but ensured a tighter, leak-proof assembly of the disks. The resulting electrode assembly was dipped in a 2 M solution of HClO$_4$ (70%, Suprapur, Merck) for 5 min and rinsed with ultrapure water just prior to its use.

For the Au/C and Au$_{AG}$ electrodes, catalyst inks were prepared by adding one part of isopropyl alcohol (99.9%, HPLC grade, Sigma-Aldrich) and three parts of ultrapure water, in that order, to a preweighed amount of Au/C or Au aerogel powder, along with the volume of Nafion solution (5 wt %, Sigma-Aldrich) needed to attain an ionomer-to-carbon or ionomer-to-aerogel mass ratio of 0.20 for Au/C vs Au$_{AG}$, respectively. Following ultrasonication, catalyst layers were prepared by depositing 10 μL of the resulting ink on the glassy carbon disk embedded in the RRDE tip, as to yield loadings of 15 vs 50 μg$_{Au}$·cm$_{geom}^{-2}$ on a gold-basis for Au/C vs Au$_{AG}$, respectively. Once dried under a running N_2 flow, these Au/C- or Au$_{AG}$-coated RRDEs (or the Au$_{PC}$ disk, minus the ink-deposition procedure highlighted above) were mounted on a Pine Research MSR Rotating Station and immersed in the N_2-saturated 0.1 M H_2SO_4 electrolyte in which all ECSA measurements were conducted. The working electrodes were immersed in the electrolyte while holding the potential at 1 V$_{RHE}$, as to avoid the uncontrolled chemisorption of SO_4^{2-} and HSO_4^- ions that compete with OH$^-$-adsorption (see eq 1 below).[48]

Following this immersion, the Au$_{PC}$ was electrochemically conditioned by potential-cycling at a sweep rate of 1000 mV·s^{-1} between 0 and 1.75 V$_{RHE}$ for 100 cycles, because in ref 49 these conditions were found to be adequate to obtain a reproducible electrode surface area. For Au$_{AG}$ and Au/C, this electrochemical conditioning was performed by cycling the potential between −0.04 and 1.64 V$_{RHE}$ at a sweep rate of 50 mV·s^{-1} for 20 cycles, during which a stable voltammogram was obtained. In contrast to the conditions used for Au$_{PC}$ (vide supra), these milder electrode conditioning parameters were chosen to avoid drastic structural changes in the nanochain network of Au$_{AG}$ and to avoid corrosion of the carbon support in Au/C. To estimate the ECSA based on the charge associated with the electrochemical reduction of the surface oxide built up at this higher inversion potential (i.e., 1.64 V$_{RHE}$), a specific charge value of 386 μC·cm$_{Au}^{-2}$ was used for normalization.[48]

Cu-UPD measurements were performed by adding to a known volume of 0.1 M H_2SO_4 electrolyte the amounts of 70 mM Cu$_2SO_4$·5H$_2$O and 70 mM NaCl solutions needed to attain electrolyte concentrations of 0.1 mM Cu^{2+} and 0.2 mM Cl$^-$, respectively. This

addition was performed while holding the working electrode at a potential of 1 V$_{RHE}$, as to avoid any unwanted Cu deposition. The purpose of adding Cl$^-$ ions was to accelerate the kinetics of the Cu-UPD reaction by facilitating coadsorption of Cu-Cl layers.[30,32] To determine the potential value below which bulk deposition of Cu starts taking place, we recorded a cathodic sweep at a scan rate of 20 mV·s^{-1} from the holding potential of 1 V$_{RHE}$ until a steep increase in the cathodic current indicative of the deposition of Cu multilayers (i.e., Cu-plating) was observed. Then, additional CVs at a rate of 20 mV·s^{-1} were recorded with different cathodic inversion potentials ($E_{inv,c}$) close to (if systematically above) the onset of the aforementioned Cu-plating. Next, to explore the effect of time on the Cu-coverage at a given potential, a potential hold was performed at selected $E_{inv,c}$ values for time durations varying from 15 to 600 s. This was immediately followed by an anodic linear sweep from the point of potential hold to 1 V$_{RHE}$, as to strip the Cu deposited during the given time. Finally, all the anodic currents thus obtained were integrated to quantify the coulombic charge associated with the stripping process. The baseline for the integration of these currents was inferred from a previous CV recorded at 20 mV·s^{-1} between 0.1 and 1 V$_{RHE}$ prior to the addition of Cu^{2+} and Cl$^-$ ions. The Cu-stripping charges were converted into ECSA values using a normalization charge of $\approx$370 μC·cm$_{Au}^{-2}$, which corresponds to the average of the equivalent charges of Cu-UPD monolayer formation on Au(111), Au(110), and Au (100) mathematically derived using the lattice parameters and packing of the surface atoms.[50]

Electrochemical Methods for IL-TEM

The experimental procedure for IL-TEM was inspired by the work of Schlögl and co-workers.[51] An experimental setup similar to that of the ECSA measurements was used, with the exception that the working electrodes consisted of Au finder-TEM grids (Ted Pella Inc.) on which 5 μL aliquots of Au/C or Au$_{AG}$ inks (1:49 diluted as compared to those used for the RDE measurements described above) had been deposited and dried under ambient conditions. These Au finder-grids were specifically chosen because of their relative stability over commonly employed copper grids and in the potential window used for electrochemical conditioning. TEM images of specific spots were acquired for these Au catalyst-Au grid ensembles, following which the outside boundary of the Au TEM grid was welded to an Au wire (99.99+%, 0.2 mm, Advent Research Materials) used to provide electrical contact for the subsequent electrochemical steps. For IL-TEM measurements investigating the effect of the electrochemical conditioning step, 20 CVs between 0.2 and 1.6 V$_{RHE}$ at 50 mV·s^{-1} were recorded on the TEM grids in 0.1 M H_2SO_4. On the other hand, IL-TEM analyses concerning the effects of CO_2-reduction conditions mimicked the respective electrochemical procedure performed on Au$_{AG}$ and Au/C during the CO_2-reduction studies (vide infra) and consisted of a 60 min hold at −0.5 V$_{RHE}$ in CO_2-saturated 0.5 M KHCO$_3$. Following the electrochemical steps, the finder-TEM grid was carefully detached from the Au wire and TEM-inspected at the same specific spots as before. This TEM analysis before and after the electrochemical procedure was performed in a JEOL JEM-ARM200F (200 kV, JEOL Limited).

Electrochemical Methods for CO$_2$-Reduction

The Au electrocatalysts were tested for their CO_2-reduction performance in an in-house developed electrochemical cell coupled to an online gas chromatograph (GC, 8610C SRI Instruments). The detailed schematic of this cell and the whole measurement setup and product quantification approaches have been discussed in our previous work.[46] Briefly, this two-compartment cell employed a perfluorinated Nafion XL membrane (Chemours) presoaked in 0.5 M KHCO$_3$ as a separator between the working and counter electrode compartments. KHCO$_3$ electrolyte (0.5 M) was first placed in a presaturation tank in which CO_2 was continuously bubbled through the electrolyte to remove dissolved O_2 and to ensure that the electrolyte was well saturated with CO_2 before injecting 3 mL of it into each cell compartment. An Ag/AgCl reference electrode (LF-1, Harvard Apparatus) stored in 3 M KCl solution was utilized for these experiments, with an $\approx$1 cm^2 area of Pt foil (99.99%, Alfa Aesar)

serving as the counter electrode. However, all potentials stated in this study are expressed against the reversible hydrogen electrode (V_{RHE}), whereby the aforementioned reference electrode was calibrated by conducting H_2-oxidation/evolution measurements on a polycrystalline Pt RDE in a H_2-saturated 0.5 M K_2HPO_4/KH_2PO_4 buffer electrolyte of the same pH as the CO_2-saturated, 0.5 M $KHCO_3$ solution. After assembling the cell and filling it with a presaturated electrolyte, high-purity CO_2 was bubbled through both compartments of the cell at a flow rate of 10 mL·min^{-1} via glass frits (ROBU, 6 mm diameter, porosity #2) for 15 min before electrochemical operation and then continuously during the electrochemical tests. All electrochemical measurements were performed using a potentiostat (VSP-300, Biologic Science Instruments) controlled by EC-Lab software (Biologic Science Instruments). The GC analyzed the CO_2-reduction gaseous products every 5 min during 1 h potential holds with the help of an autosampler function on PeakSimple 4.88. The catholyte was examined for ionic CO_2-reduction products (e.g., $HCOO^-$) at the end of every one hour potentiostatic measurement using ion chromatography (882 Compact IC Plus, Metrohm AG).

The polycrystalline Au sample used for the CO_2-electroreduction measurements was produced by sputtering an $\approx$210 nm thick layer of Au on 2.5 × 2.5 cm^2 glass plates coated with indium-doped tin oxide (ITO), with an $\approx$10 nm backing layer of chromium between the Au and ITO layers. Thus, this electrode appears referred to as Au$_{PC}$/ITO in what follows. Glassy carbon plates (Goodfellow Cambridge Limited) with an area of 2.5 × 2.5 cm^2 served as the backing electrodes on which Au/C and Au$_{AG}$ catalyst inks were drop-cast to prepare the corresponding working electrodes for CO_2RR measurements. Prior to drop-casting, the glassy carbon plates were polished on a Bühler micropolishing cloth with 0.05 μm aluminum slurry to achieve a shiny finish. Next, the plates were sonicated for 5 min each after being immersed in isopropyl alcohol and ultrapure water, respectively. Once dried, the plates were installed in a special drop-casting setup in which a PTFE gasket exposed a 1 cm^2 circular area and a 100 μg$_{Au}$·cm$_{geom}$$^{-2}$ loading of catalyst ink was deposited.[46] Once dried and before placing this glassy carbon-Au catalyst ensemble inside the cell, the catalyst layer was prewetted by transferring the electrodes into a desiccator, placing a few drops of 0.5 M $KHCO_3$ to cover the drop-casted area, and evacuating the desiccator to 30 mbar for 5 min.
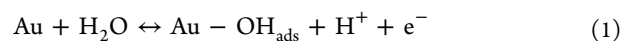
The electrochemical procedure involved performing electrochemical impedance spectroscopy measurements at open circuit in a frequency range of 1 MHz–1 Hz to determine the uncompensated solution resistance of the cell. This value varied between 50 and 60 Ω, of which 85% was compensated by EC-Lab, while the remaining 15% was accounted for during data analysis. Next, one CV was recorded at 50 mV·s^{-1} between −0.1 and 1.6 V_{RHE} followed by three CVs at 20 mV·s^{-1} in the same potential window to achieve a stable voltammogram of the Au electrocatalysts. Finally, the potential was swept from 0.1 V_{RHE} to the relevant CO_2-reduction potential, where chronoamperometric measurements for 1 h and periodic GC injections were initiated simultaneously. Following this 1 h hold, an anodic sweep at 20 mV·s^{-1} was executed to 1.6 V_{RHE} to strip off any surface species adsorbed on the catalyst surface during CO_2-reduction.[52]

■ RESULTS AND DISCUSSION

ECSA Determination of Au$_{PC}$, Au/C, and Au$_{AG}$

The meaningful comparison of a newly developed electrocatalyst with well-studied materials of different morphologies and/or architectures requires the evaluation of the ECSAs of these novel and better-established samples. While there are several electrochemical methods for determining ECSA values, their relevance and precision depend on the material under investigation and the underlying assumptions of each method.[53] Upon recording CVs of noble metals like Au, these exhibit characteristic surface oxide formation and reduction pseudocapacitive currents that have been extensively

documented in the literature and can be leveraged to calculate the ECSA of Au-based electrocatalysts.[54] In doing so, it is commonly assumed that the associated charges correspond to the chemisorption of OH on the gold surface, according to the equation:[55]

$$Au + H_2O \leftrightarrow Au - OH_{ads} + H^+ + e^- \tag{1}$$

Concomitantly, the ECSA of a given Au catalyst can be estimated by integrating the area under the peak associated with the reduction of this gold (hydr)oxide layer, as to derive the charge related to the number of surface sites electrochemically available for this oxide ad/desorption process.[54] This charge is then divided by a normalization value associated with the formation/reduction of a (hydr)oxide monolayer on an idealized Au surface, yielding the catalyst's ECSA. Herein lies the biggest shortcoming of this so-called oxide-reduction method of ECSA quantification, because the precise stoichiometry of the oxide formed at a given potential is unknown (and may imply the partial buildup of a more oxidized phase, like Au_2O_3), and it is hard to establish if this (hydr)oxide formation process is limited to a (sub)monolayer or may imply the buildup of multiple layers.[27,29]

Alternatively, the ECSA can also be quantified taking advantage of metal UPD processes, implying the potential-driven electrodeposition of (sub)monolayer amounts of metal atoms on the surface of a substrate of interest at potentials positive of the theoretical value of bulk deposition (i.e., plating) of the adsorbing species.[33] For Au-based materials, the similarity in atomic radii of Au and Cu leads to strong metal–substrate interactions that drive this UPD process, and thus Cu-UPD has been widely employed for ECSA determination of Au-based materials.[30−32] To this end, a (sub)monolayer amount of Cu is deposited on the Au surface by either cathodic potential sweep or potential hold down to/at the so-called UPD potential beyond which multilayer deposition of Cu begins to take place. This potential sweep or hold is followed by an anodic scan to strip off the adsorbed Cu adatoms. The currents associated with the deposition and stripping of Cu are subsequently integrated to obtain the deposition/stripping charge, which is in terms divided by a normalization charge for the Cu-UPD process (further discussed below) to yield the corresponding ECSA value. Most importantly, the careful experimental determination of the UPD potential at which the Cu-adsorption process reaches its maximum coverage while still being limited to a (sub)monolayer amount is crucial to ensure this method's reliability, because potential holds negative of this value result in bulk deposition (plating) of Cu on the Au surface and therefore yield overestimated ECSA values.

Based on this comparison among ECSA-determination approaches, we started our study using the surface oxide-reduction method to quantify the ECSA of Au$_{PC}$. Its voltammogram in N_2-saturated 0.1 M H_2SO_4, displayed in Figure 1a, features a characteristic, steep increase in anodic current at $\approx$1.32 V_{RHE} that leads to a broad anodic current related to the oxidation of gold and, upon inversion of the potential scanning direction, is followed by a sharper reduction peak centered at $\approx$1.16 V_{RHE}, in accordance with previous CVs recorded under the same conditions.[50,54] When the derived oxide-reduction charge is normalized by the value of 386 μC·cm$_{Au}$$^{-2}$ stated by Tremiliosi-Filho and co-workers[48] and additionally divided by the geometric surface area of the electrode (0.196 cm$_{geo}$^{2}—see the Experimental Section), a RF
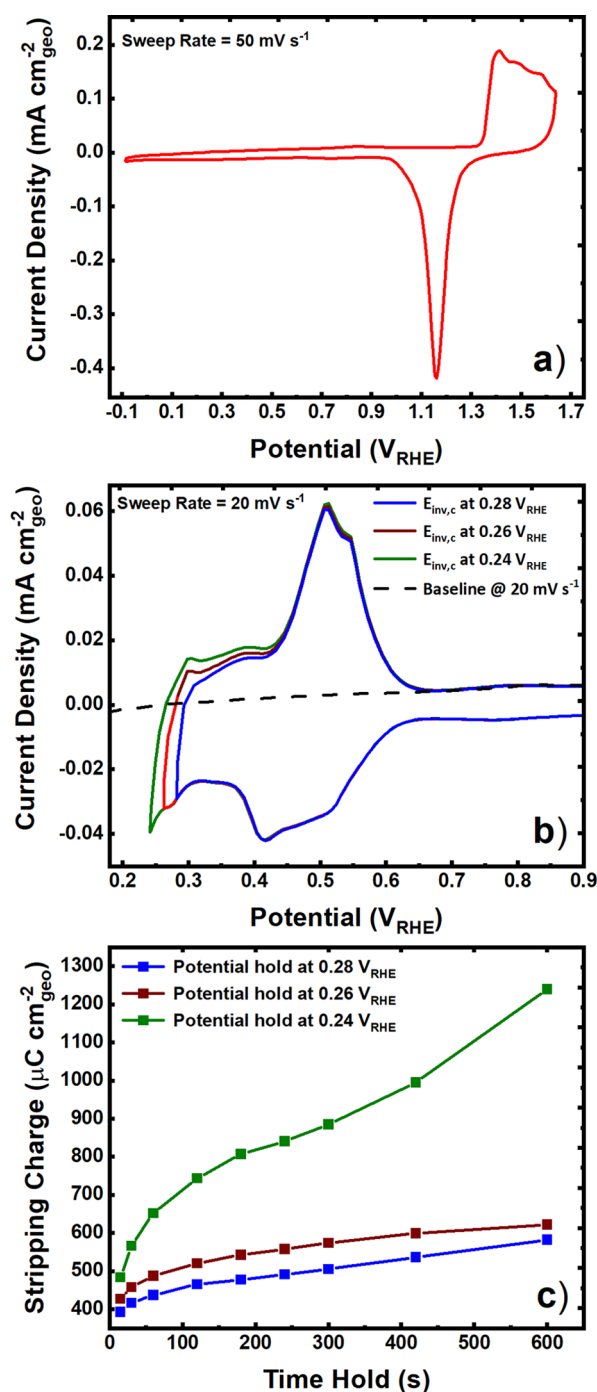
Figure 1. (a) Conditioning CVs recorded for Au$_{PC}$ in N$_2$-saturated 0.1 M H$_2$SO$_4$. (b) Cu-UPD CVs with variable cathodic inversion potentials ($E_{inv,c}$) recorded for Au$_{PC}$ in N$_2$-saturated 0.1 M H$_2$SO$_4$ + 0.1 mM CuSO$_4$.5H$_2$O + 0.2 mM NaCl. The dashed line represents the baseline for integration of Cu stripping peaks. (c) Cu stripping charges calculated from anodic scans after chronoamperometric holds at the potentials shown in plot (b) for different time durations.

of ≈1.7 cm$_{Au}$$^{-2}$·cm$_{geo}$$^{-2}$ is estimated for Au$_{PC}$ and appears listed in Table 1. This RF is in line with the values reported for other Au$_{PC}$ electrodes (cf. 1.6 vs 2.1 cm$_{Au}$$^{-2}$·cm$_{geo}$$^{-2}$ in refs 48 vs 56, respectively) and generally agrees with what would be expected for polycrystalline surfaces prepared by hand-polishing.[57,58]

After this initial RF-quantification for Au$_{PC}$ based on the oxide-reduction method, we proceed to conduct a more reliable RF-determination using Cu-UPD. For this, CVs in the same 0.1 M H$_2$SO$_4$ electrolyte additionally containing 0.1 mM Cu^{2+} and 0.2 mM Cl$^-$ were first recorded with cathodic inversion potentials ($E_{inv,c}$) of 0.28, 0.26, or 0.24 V$_{RHE}$ (see Figure 1b). For potentials ≤0.24 V$_{RHE}$, a steep increase in cathodic current was observed, indicating the unambiguous occurrence of Cu-plating. Following this, potentiostatic Cu-UPD measurements were conducted at the aforementioned $E_{inv,c}$ values, and the Cu-stripping charges recorded in the subsequent anodic sweeps appear plotted in Figure 1c as a function of the duration of the potential hold. Evidently, the chronoamperometric measurements performed at 0.24 V$_{RHE}$ resulted in a monotonic increase of the Cu-stripping charge with potential-hold time indicative of a bulk Cu-deposition process. On the contrary, potential-holding at 0.28 and 0.26 V$_{RHE}$ led to Cu-stripping charges plateauing over a time interval of 600 s, indicating the occurrence of a Cu-UPD process and the formation of a Cu-(sub)monolayer on the Au$_{PC}$ surface. Using the normalization charge of ≈370 μC·cm$_{Au}$$^{-2}$ and considering the Cu stripping charge of ≈622 μC·cm$_{geo}$$^{-2}$ achieved for the UPD potential of 0.26 V$_{RHE}$ result in a RF of ≈1.6 cm$_{Au}$^{2}·cm$_{geo}$$^{-2}$, commensurate with the value of ≈1.7 cm$_{Au}$^{2}·cm$_{geo}$$^{-2}$ derived using the oxide-reduction method, and that also appears tabulated in Table 1. Notably, when this RF-quantification is performed on the basis of the Cu-stripping charge in the corresponding CV measurement with an $E_{inv,c}$ of 0.26 V$_{RHE}$ (i.e., as opposed to using the stripping charge following a sufficiently long E-holding), the result is an RF of 1.1 cm$_{Au}$^{2}·cm$_{geo}$$^{-2}$ (cf. Table 1).

This ≈31% lower value highlights the importance of performing these Cu-UPD measurements using potentiostatic holds followed by anodic scans, as opposed to the CV measurements applied in previous CO$_2$-reduction studies (vide supra) which, as we will further discuss below, lead to underestimated surface areas and correspondingly overestimated SSAs.

Having assessed the ECSA of Au$_{PC}$, we performed a similar ECSA-quantification study on the commercial, 20% Au/C catalyst. The TEM images of this material shown in Figure 2a unveil that its nanoparticles exhibit an average particle size of ≈9 nm. Approximating these Au nanoparticles as spheres, we leveraged a particle size distribution (see Figure S1) derived from 200 samplings in the TEM images and calculated a specific surface area of ≈27 m^2·g$_{Au}$$^{-1}$ for the Au/C catalyst (see section 1 in the Supporting Information for details) that again appears summarized in Table 1.[59]

Upon subsequent electrochemical measurements with a gold loading of 15 μg$_{Au}$·cm$_{geo}$$^{-2}$ in N$_2$-saturated 0.1 M H$_2$SO$_4$, this Au/C catalyst displayed the characteristic CV displayed in Figure 3a which, compared to the CV of Au$_{PC}$ in Figure 1a, features a broad double-layer current caused by the additional presence of carbon that is in line with previous observations.[60] Similar to the case of Au$_{PC}$, the charge under the Au oxide reduction peak in Figure 3a is normalized by a specific charge of 386 μC·cm$_{Au}$$^{-2}$ and further divided by the geometric surface area of the electrode (0.196 cm$_{geo}$^{2}) and the catalyst ink loading (15 μg$_{Au}$·cm$_{geom}$$^{-2}$) to yield an ECSA value of ≈21 m^2·g$_{Au}$$^{-1}$ listed again in Table 1.

Once we obtained a reproducible CV for Au/C in N$_2$-saturated 0.1 M H$_2$SO$_4$, Cu^{2+} and Cl$^-$ ions were added to the electrolyte (see the Experimental Section), and the potential was cycled from 1 V$_{RHE}$ to varying $E_{inv,c}$ potentials of 0.30, 0.28, 0.26, or 0.24 V$_{RHE}$ to achieve varying levels of Cu-deposition

Table 1. Summary of RF ($cm_{Au}^2\ cm_{geo}^{-2}$) and ECSA ($m^2 \cdot g_{Au}^{-1}$) Values Derived for Au_{PC}, Au/C, and Au_{AG} Using TEM, Au Oxide Reduction, and Cu-UPD Methods (E-Scan and E-Hold + Stripping)

	TEM[a]	Au oxide reduction	Cu-UPD, E-scan	Cu-UPD, E-hold + stripping
Au_{PC}[b]		$1.7\ cm_{Au}^2 \cdot cm_{geo}^{-2}$	$1.1\ cm_{Au}^2 \cdot cm_{geo}^{-2}$	$1.6\ cm_{Au}^2 \cdot cm_{geo}^{-2}$
Au/C	$27\ m^2 \cdot g_{Au}^{-1}$	$21\ m^2 \cdot g_{Au}^{-1}$	$10\ m^2 \cdot g_{Au}^{-1}$	$17\ m^2 \cdot g_{Au}^{-1}$
Au_{AG}		$11\ m^2 \cdot g_{Au}^{-1}$	$2\ m^2 \cdot g_{Au}^{-1}$	$9\ m^2 \cdot g_{Au}^{-1}$

[a]Only applicable to the Au/C sample. [b]For Au_{PC}, the tabulated values are RFs corresponding to the ratio between the surface area of Au and the geometric area of the electrode.
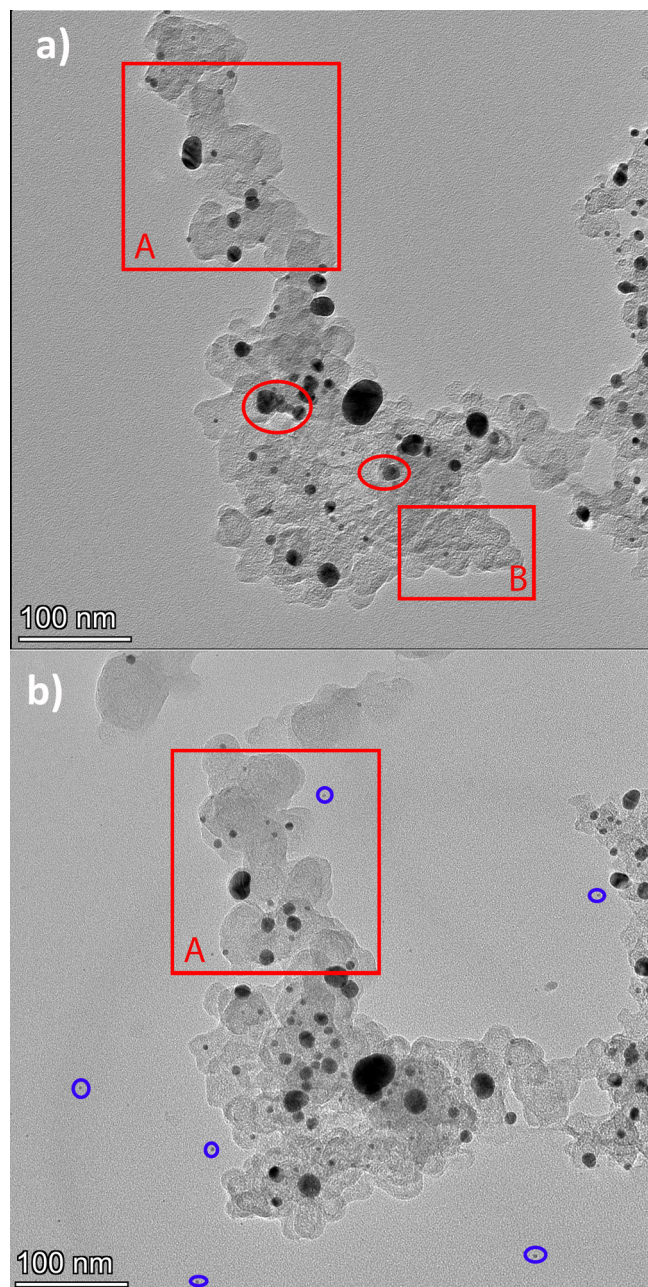
Figure 2. IL-TEM images before (a) and after (b) conducting 20 cyclic voltammetry scans at 50 mV.s^{-1} on Au/C between 0.2 and 1.6 V_{RHE} in N$_2$-saturated 0.1 M H$_2$SO$_4$.

on the Au-nanoparticles' surface. These CVs are displayed in Figure 3b, and the corresponding chronoamperometric and stripping CV measurements used to determine the accurate UPD potential appear plotted in Figure 3c. Unlike in the case of Au_{PC}, in which bulk Cu-deposition was only observed at

potentials $\leq 0.24\ V_{RHE}$ (see Figure 2b), for Au/C this effect is already present at 0.26 V_{RHE}, and Cu-stripping charges independent of the potential hold duration (and thus indicative of the exclusive occurrence of a UPD process) are only observed for $E_{inv,c}$ values of 0.28 or 0.30 V_{RHE}. Most importantly, if one considers the Cu-stripping charge of ≈ 954 $\mu C \cdot cm_{geo}^{-2}$ obtained following a 600 s hold at 0.28 V_{RHE}, along with the Cu-UPD normalization charge of 370 $\mu C \cdot cm_{Au}^{-2}$ discussed above, an ECSA value of $\approx 17\ m^2 \cdot g_{Au}^{-1}$ is estimated (see Table 1). Interestingly, this ECSA is $\approx 40\%$ lower than the specific surface area of $\approx 27\ m^2 \cdot g_{Au}^{-1}$ estimated on the basis of the nanoparticles' size distribution and mentioned above, a disagreement that stems from fractions of these nanoparticles that are not accessible to the electrolyte and thus do not contribute to the electrochemical process (e.g., due to their partial agglomeration and/or anchoring to the support surface),[61] and is in accordance with what has been reported in previous literature for C-supported metal nanoparticles.[59,62] Furthermore, when this ECSA quantification is performed using the Cu-stripping charge from continuous CVs with the same $E_{inv,c}$ value as the UPD potential deduced above (i.e., 0.28 V_{RHE}), it results in an ECSA value of 10 $m^2 \cdot g_{Au}^{-1}$ (cf. Table 1). This large deviation of $\approx 40\%$ with regard to the Cu-UPD measurements performed with potential holds is in line with the behavior observed above for Au_{PC} and again emphasizes the downsides of UPD measurements in a potentiodynamic mode.

After establishing the ECSA of this Au/C benchmark electrocatalyst, we shift our focus to the novel 3D Au aerogel (Au_{AG}). The TEM images displayed in Figure 4a unveil that the unsupported Au network consists of a nanostructure of smooth, interconnected chains with an average web thickness of ≈ 5 nm and numerous junctions with a larger average diameter. Notably, these irregular dimensions and abundant interconnectivity are in contrast with the observations for Pt-based aerogels, consisting of a necklace of nanoparticles of relatively resembling diameters and with a lower interconnectivity extent, and prevent a reliable estimation of the geometric surface area of this Au_{AG} sample based on its necklace's bare average diameter.[63,64]

The ECSA determination of the Au_{AG} was pursued in a similar manner to that for Au/C, in this case by preparing RDEs with an aerogel loading of 50 $\mu g_{Au} \cdot cm_{geo}^{-2}$ and recording CVs in N$_2$-saturated 0.1 M H$_2$SO$_4$. These are featured in Figure 5a and display a narrow double-layer region (consistent with the Au_{PC} CVs—see Figure 1a) compared to the Au/C voltammograms in Figure 3a that can be ascribed to the absence of a carbon support in the aerogels. Leveraging the Au oxide reduction method for ECSA determination of this 50 $\mu g_{Au} \cdot cm_{geo}^{-2}$ Au aerogel catalyst layer, we obtain an ECSA value of $\approx 11\ m^2 \cdot g_{Au}^{-1}$, which appears tabulated in Table 1.

On similar lines to Au_{PC} and Au/C, we performed Cu-UPD measurements on Au_{AG} by introducing Cu^{2+} into the
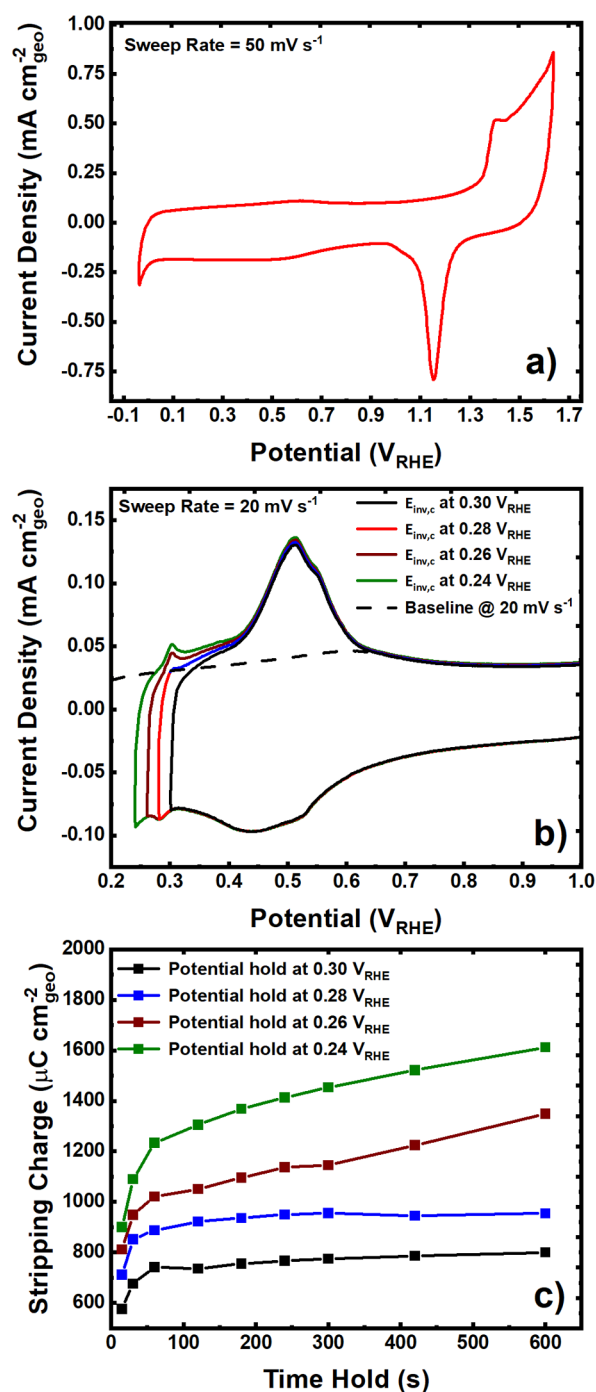
Figure 3. (a) Conditioning CVs recorded for Au/C in N_2-saturated 0.1 M H_2SO_4. (b) Cu-UPD CVs with variable cathodic inversion potentials ($E_{inv,c}$) recorded for Au/C in N_2-saturated 0.1 M H_2SO_4 with 0.1 mM $CuSO_4 \cdot 5H_2O$ and 0.2 mM NaCl. The dashed line represents the baseline for integration of Cu stripping peaks. (c) Cu stripping charges calculated from anodic scans after chronoamperometric holds at the potentials shown in plot (b) for different time durations.

Figure 4. IL-TEM images before (a) and after (b) conducting 20 cyclic voltammetry scans at 50 mV s^{-1} on Au_{AG} between 0.2 and 1.6 V_{RHE} in N_2-saturated 0.1 M H_2SO_4.

experimental setup; notably, these measurements were conducted without adding Cl^-, because in a series of separate measurements we observed that this anionic species leads to a continuous decline of the Cu-stripping charge (see Figure S2) that we attribute to a Cl^--induced pitting of the aerogel's Au nanochains which might result in the collapse of their 3D nanostructure and drastically reduce this material's ECSA.[65,66]
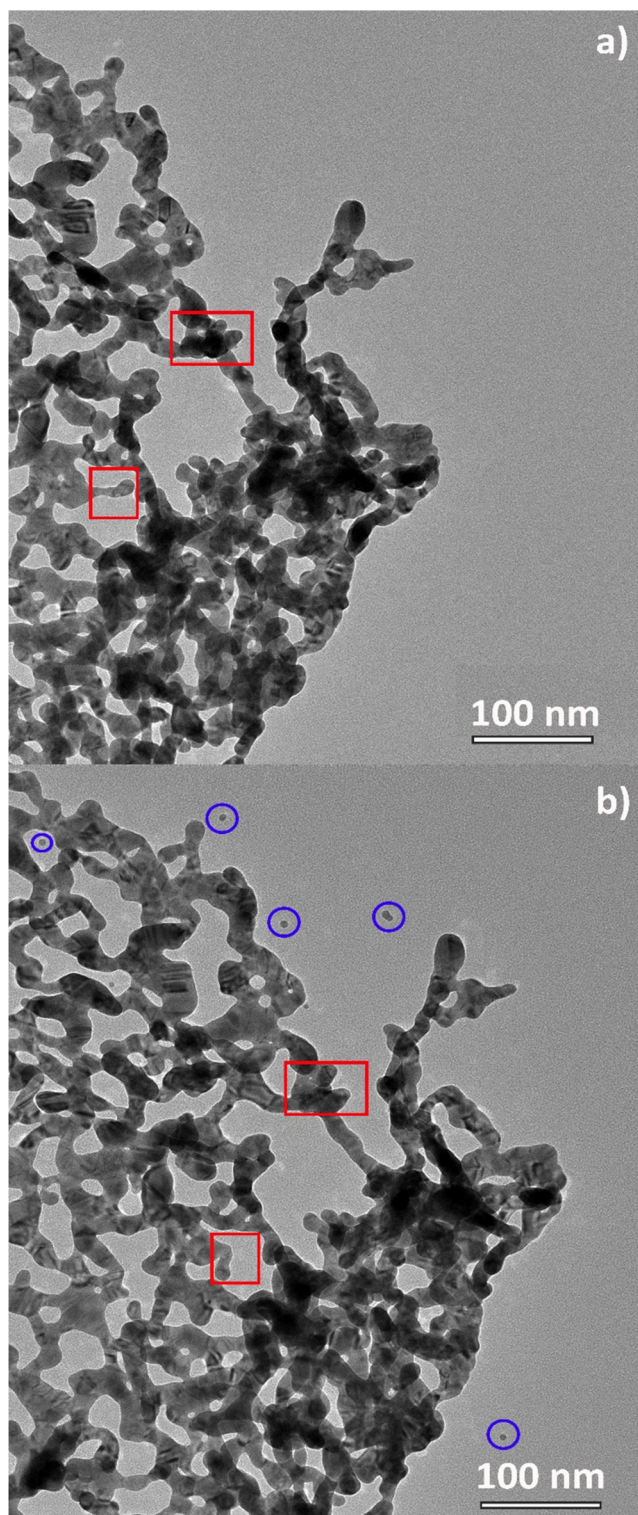
Following this preliminary observation, we conducted potential-sweep and -hold measurements sequentially to determine the UPD potential and associated Cu-stripping charges; these results are presented in Figure 5b,c, respectively. Considering the Cu-stripping charge of $\approx 1745 \ \mu C \cdot cm_{geo}^{-2}$ obtained after a 600 s hold at a UPD potential of 0.26 V_{RHE}, along with a Cu-UPD normalization charge of 370 $\mu C \cdot cm_{Au}^{-2}$,
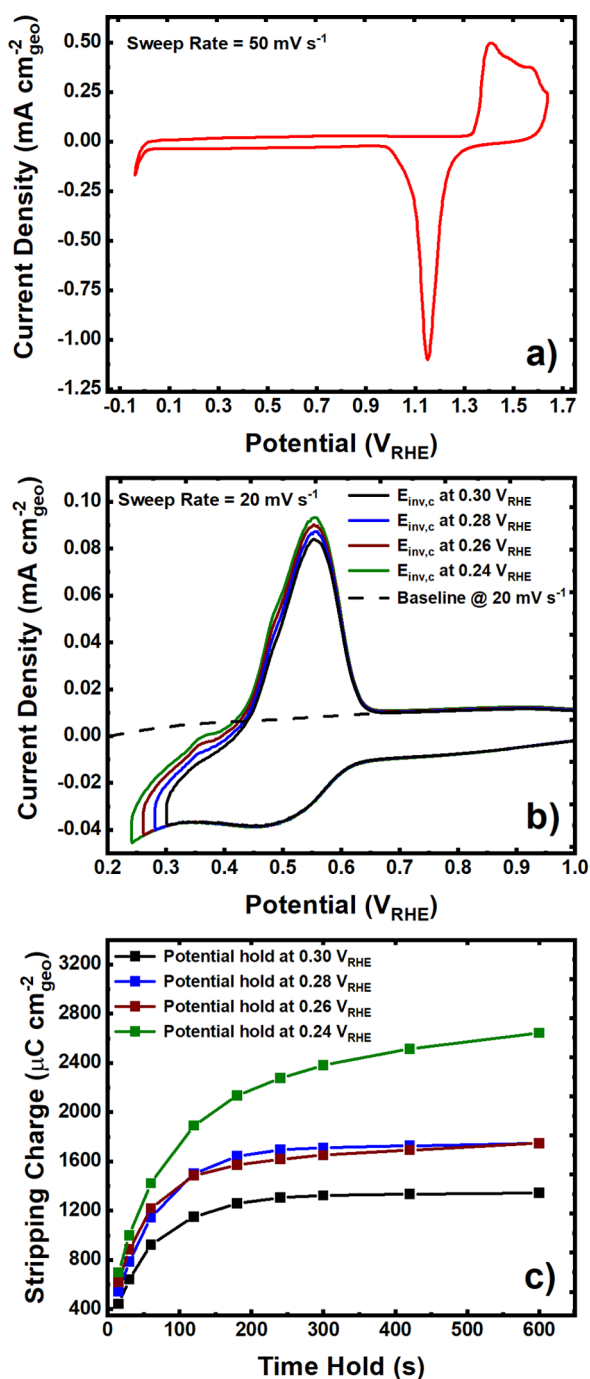
Figure 5. (a) Conditioning CVs recorded for Au_{AG} in N_2-saturated 0.1 M H_2SO_4. (b) Cu-UPD CVs with variable cathodic inversion potentials ($E_{inv,c}$) recorded for Au_{AG} in N_2-saturated 0.1 M H_2SO_4 with 0.1 mM $CuSO_4.5H_2O$. The dashed line represents the baseline for integration of Cu stripping peaks. (c) Cu stripping charges calculated from anodic scans after chronoamperometric holds at the potentials shown in plot (b) for different time durations.

a catalyst loading of 50 $\mu g_{Au}\cdot cm_{geo}^{-2}$, and a geometric area of 0.196 cm^2, we obtain the ECSA value of ≈ 9 $m^2\cdot g_{Au}^{-1}$ listed in Table 1. By comparison, the CV-based Cu-UPD measurement for the same UPD potential of 0.26 V_{RHE} results in an ECSA value of only ≈ 2 $m^2\cdot g_{Au}^{-1}$, which is $\approx 80\%$ lower than what is derived from the equivalent Cu-UPD measurements with potential hold. Moreover, this difference between ECSA values derived from both Cu-UPD methods (i.e., with continuous E-

scanning vs holding the potential) is in terms ≈ 2-fold larger than what we observed in the above Au/C and Au_{PC} measurements (see Table 1). A likely reason for this could be the absence of Cl^- ions during Cu-UPD experiments with the Au aerogel, as compared to those performed on Au_{PC} and Au/C, because this absence of chloride likely results in slower Cu-deposition kinetics. Most importantly, the majority of the studies discussed above in which Cu-UPD CVs were used to estimate Au-nanomaterials' ECSAs also overlooked the inclusion of Cl^- in their UPD measurements and, based on these observations, likely reported largely underestimated ECSAs.[17,18,67] Notably, we believe that this issue can be likely aggravated if the Cu-UPD CVs are recorded at faster scan rates.[17]

In summary, under the assumption that the Cu-UPD method based on potential holds yields the most reliable ECSA values, Table 1 unveils that the Au oxide reduction method slightly overestimates (by ≈ 10 to 20%) the ECSAs of all three materials discussed in this work. On the other hand, the Cu-UPD method, which employs potentiodynamic deposition of Cu, consistently underestimates the ECSAs, and alarmingly so when the measurements are conducted in the absence of Cl^- ions.

IL-TEM Analysis for Electrochemical Conditioning

The electrochemical conditioning of Au surfaces involves potential-cycling to high anodic potentials (≥ 1.6 V_{RHE}) that can lead to surface reconstruction, Au dissolution, and/or redeposition[66,68,69] and may alter the surface area estimated using the oxide-reduction and Cu-UPD methods applied above. To determine the extent to which these effects may have impacted the ECSA values reported in Table 1, we employed IL-TEM to gain microscopic insight regarding the morphology of the nanostructured Au electrocatalysts before and after conditioning (i.e., potential-cycling). These IL-TEM measurements were performed on both Au/C and Au_{AG} by mimicking the electrochemical conditioning steps performed in the RDE configuration (i.e., recording 20 CVs at 50 mV·s^{-1} between 0.2 and 1.6 V_{RHE} in N_2-saturated 0.1 M H_2SO_4—see Figure S3), and the corresponding IL-TEM images before and after conditioning are presented in Figures 2a,b and 4a,b, respectively. For Au/C, the red squares marked as 'A' in Figure 2a,b depict how an elongated part of the carbon matrix gets crumpled into a smaller volume after cyclic voltammetry, while the red square marked 'B' points a part of carbonaceous material that is absent in the postmortem TEM image. These observations hint toward considerable mobility and corrosion of the carbon matrix at these high anodic potentials, consistent with what has been reported previously.[70] Because the Au NPs are embedded in the carbon matrix, its corrosion results in the nanoparticles' migration and even detachment, as indicated by the red circles in Figure 2a (absent in the postconditioning image, cf. Figure 2b). Interestingly, the blue circles in Figure 2b point at the appearance of ≈ 3 nm Au NPs in the vacant region around the carbon matrix that cannot be found in Figure 2a. We hypothesize that these smaller Au NPs were produced as a result of Au dissolution and redeposition as the Au/C was cycled between oxidative and reductive potentials.[71] While the relocation of NPs should not affect the overall ECSA of the Au/C electrocatalyst, their segmentation and possible coalescence would lead to a change in the ECSA. To estimate the impact of these potential-cycling effects on this variable, we evaluated the catalyst's postconditioning particle size distribu-

tion using the same procedures highlighted above and discussed it in section 1 of the SI (see Figure S1b), from which we derived an average particle size of ≈9.5 nm and a corresponding geometric surface area of ≈24 $m^2 \cdot g_{Au}^{-1}$. Comparing this value to the preconditioning geometric surface area of ≈27 $m^2 \cdot g_{Au}^{-1}$ and considering the error associated with such statistically averaged calculations, these conditioning-induced changes in the surface area can be considered negligible.

Next, we shift our focus to the IL-TEM images of Au_{AG} in Figure 4b, whereby a cursory glance reveals that the overall 3D structure looks largely unchanged, pointing toward an enhanced stability of this unsupported electrocatalyst during electrode conditioning. However, similar to what was observed for Au/C, the blue circles in the postconditioning TEM images in Figure 4b indicate the presence of ≈3 to 4 nm Au NPs around the Au_{AG} that were absent in the TEM images of the as-prepared Au_{AG} in Figure 4a.

Therefore, these Au NPs were also produced because of the Au dissolution−redeposition cycles caused by potential cycling; based on the above conclusions for Au/C, though, we also assume that their appearance does not have a significant effect on the material's ECSA. Additionally, the red squares in Figure 4a,b point out minute changes observable in the aerogel network, whereby chain terminations are notably different or the spacing between the chains has changed. On the other hand, this reshaping of the aerogel network is highly localized and does not entail any significant changes in the necklace size, and thus we believe that the electrochemical conditioning does not lead to significant changes in the material's ECSA.

CO$_2$-Reduction Performance of Au$_{PC}$/ITO, Au/C, and Au$_{AG}$

Following this rigorous quantification of the nanocatalysts' ECSA and the verification that this key parameter is not significantly affected by their electrochemical conditioning, we tested the CO$_2$-reduction performance of Au$_{PC}$/ITO, Au/C, and Au$_{AG}$ in CO$_2$-saturated 0.5 M KHCO$_3$. The FEs for CO and H$_2$ production (blue vs red symbols) during CO$_2$-reduction on Au$_{AG}$ and Au/C at various potentials are shown in Figure 6a,b, respectively, while the corresponding results for Au$_{PC}$/ITO are displayed in Figure S4. Regarding the latter, the current densities recorded during CO$_2$-reduction on Au$_{PC}$/ITO at potentials > −0.5 V$_{RHE}$ were too low to generate CO and H$_2$ at levels that can be accurately and reliably detected by the GC, and thus these potentials have been omitted from Figure S4. Qualitatively speaking, the FE and CO partial current trends observed for Au$_{PC}$/ITO are very similar to those reported by Kuhl et al. for polycrystalline Au. More specifically, both polycrystalline samples show a peak FE$_{CO}$ at ≈−0.7 V$_{RHE}$, but higher CO partial currents are reported by Kuhl et al. at moderate overpotentials than our Au$_{PC}$/ITO (Figure S5).[72] On the other hand, while the CO partial current trends observed by Hori et al. are qualitatively similar to our findings as well, the peak FE$_{CO}$ in Hori's study occurs at a much lower potential of ≈−0.92 V$_{RHE}$.[9] We hypothesize that these differences may stem from inconsistencies in the experimental setups used in those studies versus this work; specifically, Kuhl and co-workers used a two-compartment cell similar to ours but with CO$_2$-saturated 0.1 M KHCO$_3$ as the electrolyte, while Hori et al. also used 0.5 M KHCO$_3$, yet in a three-compartment cell with the cathode at its center (and thus under different convection conditions).[46]
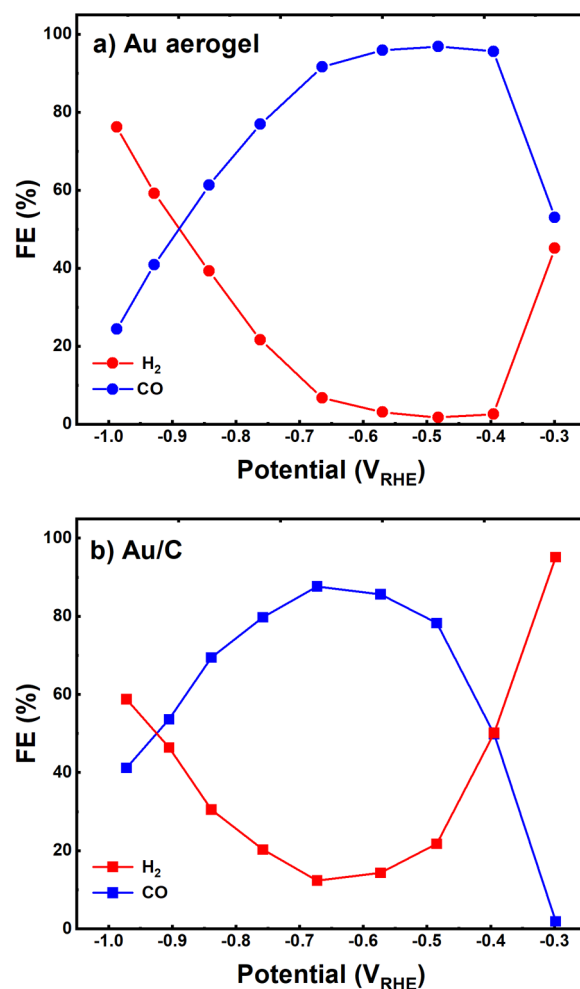

Figure 6. FE of CO (blue) and H$_2$ (red) produced during CO$_2$-reduction on (a) 100 $\mu g \cdot cm^{-2}$ Au aerogel and (b) 100 $\mu g \cdot cm^{-2}$ Au/C (Au basis) in CO$_2$-saturated 0.5 M KHCO$_3$, respectively.

On the other hand, the FEs for Au$_{AG}$ and Au/C exhibit quite similar qualitative trends at moderate to low potentials (i.e., ≤ −0.6 V$_{RHE}$), with CO production being predominant down to ≈−0.8 V$_{RHE}$ and H$_2$ production taking over as the applied potential becomes more negative (see Figure 6a,b). Additionally, both Au/C and Au$_{AG}$ produced negligible amounts of HCOO$^-$ over the whole potential range (< 1%, and hence not shown), which is in accordance with the literature.[73] Moreover, Au$_{AG}$ proves to be more selective than Au/C for CO production, achieving a peak FE of ≈97% for this product at ≈−0.48 V$_{RHE}$, as compared to the maxima of ≈88% vs ≈83% at ≈−0.67 vs ≈−0.69 V$_{RHE}$ for Au/C vs Au$_{PC}$/ITO, respectively. Specifically when it comes to the comparison between nanomaterials (i.e., Au$_{AG}$ vs Au/C), this behavior may stem from a suppression of the competing H$_2$-evolution reaction (HER) at high-to-medium potentials on the unsupported Au aerogel, in terms caused by the absence of an HER-active carbon phase in this material. To validate this hypothesis, we performed additional electrochemical measurements in CO$_2$-saturated 0.5 M KHCO$_3$ on a working electrode made of the (Au-free) Vulcan XC-72 carbon black, with a carbon loading of 400 $\mu g_C \cdot cm^{-2}$ equivalent to the one in the Au/C measurements. Notably, H$_2$ was the only reduction product detected in these measurements, and the H$_2$ partial currents for this C-electrode as well as Au$_{AG}$ and Au/C are

displayed in Figure 7a. As shown in the figure's inset, these H_2 partial currents at potentials ≥ -0.6 V_{RHE} in which the reaction
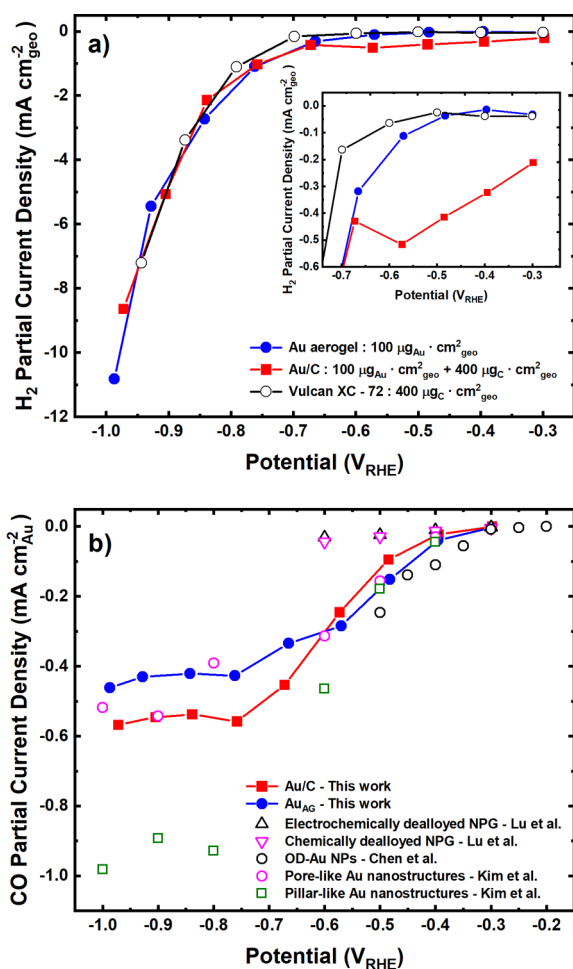

Figure 7. (a) Partial current densities of H_2, normalized with respect to the geometric area, generated during CO_2-reduction of Au_{AG}, Au/C, and Vulcan XC-72 in CO_2-saturated 0.5 M $KHCO_3$, with the inset showing the zoomed-in picture of partial currents in the kinetically controlled regime and (b) partial current densities of CO, normalized with respect to the ECSA, generated during CO_2-reduction on materials reported in this study and in the literature.

is expected to proceed mostly under kinetic control are 5−8 times higher for Au/C as compared to the Au-free, C-electrode despite the identical carbon loadings in both measurements. Thus, the high H_2 partial currents featured by the Au/C sample do not stem from its C-support, contradicting our initial assumption that the higher FE_{H2} for Au/C vs Au_{AG} at low overpotentials was a result of the presence of a carbon support in the former. Instead, the low H_2 selectivity observed for Au_{AG} over Au/C likely stems from an effect of the Au-nanoparticle shape and size on the HER-kinetics, whereby the smaller particles (i.e., higher ECSA) of the Au/C catalyst vs Au_{AG} promote this undesired side-reaction.[14,34]

Finally, we assess the possible occurrence of particle size/shape effects on the CO_2-to-CO SSA of these nanocatalysts by plotting their potential-dependent, ECSA-normalized CO partial currents. To this end, the CO-specific current densities were normalized with respect to the ECSAs determined by the oxide-reduction method in the same electrochemical cell in which the samples were tested for CO_2-electroreduction. The

ECSA values thus obtained were ≈ 15 $m^2 \cdot g_{Au}^{-1}$ for Au/C and ≈ 12 $m^2 \cdot g_{Au}^{-1}$ for Au_{AG}. While the value obtained for Au_{AG} is quite similar to the one obtained with the same method in 0.1 M H_2SO_4 in an RDE setup (≈ 11 $m^2 \cdot g_{Au}^{-1}$; refer to Table 1), a significant decline in the ECSA is observed for Au/C (as compared to ≈ 21 $m^2 \cdot g_{Au}^{-1}$ in the RDE setup) which may be attributed to the presence of 6.6 times more loading and thus, underutilization of the thicker catalyst layer (consistent with our previous observations for a carbon-supported Pd-catalyst).[46] Figure 7b reveals that Au_{AG} and Au/C feature similar ECSA-normalized, CO partial currents across the potential range within which their performance appears to be under kinetic control (corresponding to potentials ≥ -0.6 V_{RHE} and CO-currents ≤ -0.25 $mA \cdot cm_{Au}^{-2}$), while larger deviations are observed at lower potentials at which these partial currents reach a plateau, likely caused by a limited supply of reactant stemming from insufficient convection and/or surface poisoning.[13,49,52]

Figure 7b also includes a comparison with other Au-based nanomaterials reported elsewhere, chosen considering the similarities among the geometry of the electrochemical cell and experimental conditions employed. Among these, Lu and co-workers' nanoporous gold and Chen and co-workers' oxide-derived Au-NPs[16,17] feature CO partial currents that are higher than those of Au/C and Au_{AG} when assessed on a geometric area basis (see Figure S5). However, upon normalizing both currents with respect to the Au-ECSA values reported in the same studies, we find that the resulting CO-SSAs are lower or similar to those featured by Au_{AG} and Au/C, respectively (see Figure 7b). While the nanostructure width of the pore-like and pillar-like nanostructures reported by Kim et al. is 4−10 times higher (≈ 20 to 30 and ≈ 50 nm, respectively) than the nanomaterials used in this study, these materials qualitatively resemble the network-like structure of Au_{AG} when observed under the microscope, and hence, are ideal candidates for comparison to our materials.[18] Moreover, as also seen in Figures 7b and S5, the ECSA- and geometric-surface-normalized partial CO-currents reported by Kim and co-workers for pore-like Au nanostructures that qualitatively resemble the network-like structure of our Au_{AG} are well in accordance with the CO partial current density values reported herein for Au_{AG} and Au/C within the low-current regime associated with kinetic control. On the other hand, significant deviations can again be observed at higher current densities at which mass transport limitations within the catalyst layer start becoming an important factor. Thus, this analysis indicates that the performance of this highly CO-selective Au_{AG} is in line with the trends reported in the past and ultimately points at an absence of particle size effects on the CO_2-to-CO selectivity of such Au nanostructures, at least within the size ranges considered in this work and the studies included in the above comparison.

IL-TEM Analysis for the CO_2RR

To finalize this work, and inspired by previous studies reporting significant morphological changes in Au-based catalysts in the course of CO_2RR,[74−76] we performed an IL-TEM analysis of the Au_{AG} and Au/C samples before and after CO_2-reduction. The experimental setup is similar to that employed during IL-TEM analysis for electrochemical conditioning and the electrochemical protocol mimics that were used during CO_2-reduction measurements at -0.5 V_{RHE}, the potential leading to the highest CO FE in the GC cell (see
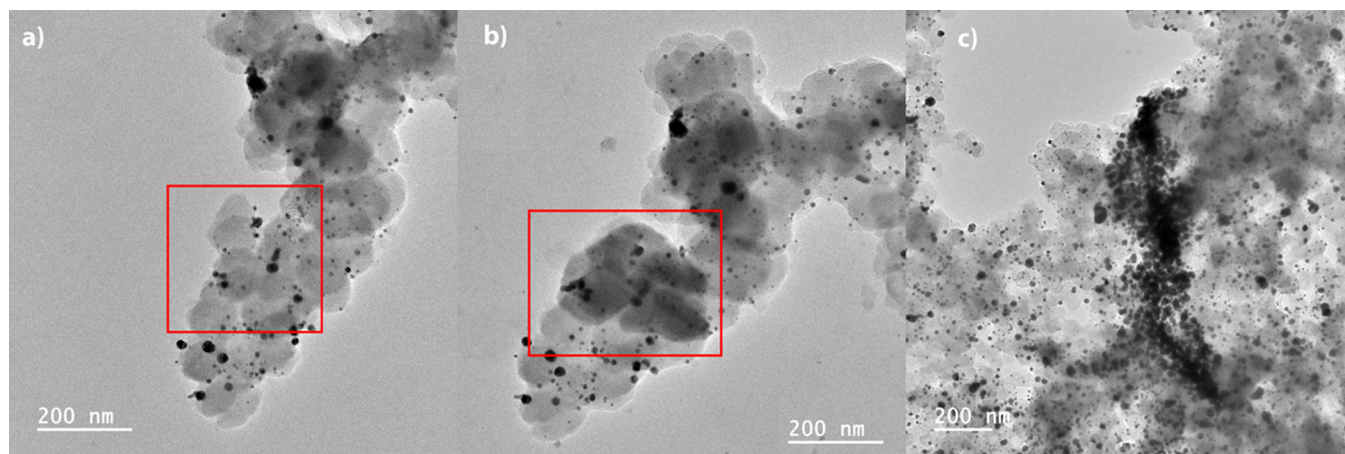
Figure 8. IL-TEM analysis performed on Au/C (a) before and (b) after CO_2-reduction at -0.5 V_{RHE} in CO_2-saturated 0.5 M $KHCO_3$. The red squares serve as a guide to the eye to point out changes that have taken place. (c) TEM image acquired after CO_2-reduction at -0.5 V_{RHE} for 1 h, showing significant coalescence of Au NPs around one spot.
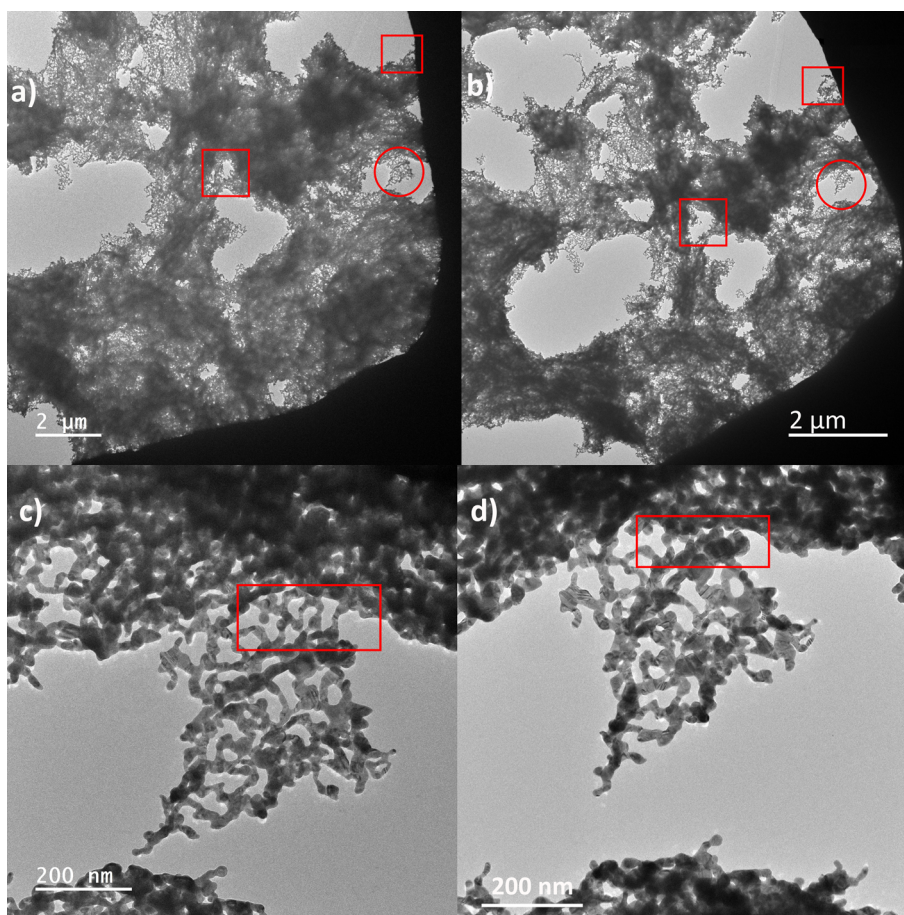

Figure 9. IL-TEM analysis performed on Au_{AG} (a), (c) before and (b), (d) after CO_2-reduction at -0.5 V_{RHE} in CO_2-saturated 0.5 M $KHCO_3$. The red squares serve as a guide to the eye to point out changes that have taken place and the red circles in (a) and (b) are zoomed into (c) and (d), respectively.

Figure 6).The IL-TEM results for Au/C are shown in Figure 8, whereby the image in Figure 8a was acquired before the entire electrochemical protocol for CO_2-reduction (conditioning CVs and potential holds), and that in Figure 8b was acquired afterward. At a nanoscale, no significant changes are observed apart from the folding of a part of the carbon scaffold on itself, indicated by the red box. A more drastic change is shown in

Figure 8c, though, whereby significant coalescence of numerous Au NPs in one spot is observed after 1 h CO_2-reduction hold at -0.5 V_{RHE}. Such occurrences were not observed in the sample prior to the CO_2-reduction test and, while they are relatively rare, this agglomeration is in accordance with what has been observed in the literature for Au NPs deposited on C supports.[77]

Complementarily, the IL-TEM results for Au_{AG} are shown in Figure 9. A low-magnification view of the aerogel's structure is presented in Figure 9a,b, where no significant changes can be seen apart from some modifications in the way the Au network folds on itself, leading to changes in pore sizes (red squares). The red circles in these images are zoomed in and shown in Figure 9c,d, which prove that the aerogel preserves the ligament nanostructure during the CO_2RR. A minor change is highlighted by the red box, where a part of the aerogel in Figure 9c cannot be seen any more in the post-CO_2RR image in Figure 9d, because it folded into the bulk of the aerogel. Despite this minor change, this general stability of the Au aerogel nanoarchitecture over the commercially available Au NPs embedded in the carbon support during the CO_2RR can be attributed to an inherent metastability of the said aerogel, consistent with previous reports in which Au NPs tend to assemble in a nanochain-like structure very similar to this aerogel upon the CO_2RR.[75,76]

CONCLUSIONS

In summary, we examined polycrystalline Au, Au on carbon, and unsupported Au aerogels for their ECSAs using the surface oxide-reduction and Cu-UPD methods and found that the potential-hold Cu-UPD measurements provide a much more reliable ECSA quantification as compared to the often-employed potential-sweep Cu-UPD method. IL-TEM analysis performed before and after electrochemical conditioning suggested the occurrence of dissolution and redeposition of Au in the nanostructured Au catalysts, but this is shown to not affect the ECSAs drastically. Despite its lower ECSA, the Au aerogel featured similar ECSA-normalized CO partial current densities and recorded higher FE for CO production as compared to Au/C over the entire potential range, with a peak FE_{CO} of ≈97% at ≈−0.48 V_{RHE}. The suppression of H_2 evolution during the CO_2RR exhibited by the Au aerogel as compared to Au/C is proven to be an effect of the Au-nanoparticle size and shape and not an effect of the absence of a carbon support. Finally, IL-TEM investigation before and after the CO_2RR suggests that the Au aerogel is stable during the process and does not undergo significant structural changes. By exploring the CO_2-reduction prospects of novel Au aerogel architectures, this work provides a basis for benchmarking future electrochemical investigations involving Au-based (unsupported) nanostructures.

ASSOCIATED CONTENT

Supporting Information

The Supporting Information is available free of charge at https://pubs.acs.org/doi/10.1021/acsmaterialsau.1c00067.

> Specific surface area calculations from particle size distributions for Au/C, CVs showing pitting of Au_{AG} in the presence of Cl^-, CVs recorded at the end of IL-TEM measurements, FE trends for the CO_2RR on Au_{PC}/ITO, and geometric surface area-normalized CO partial current densities for the CO_2RR on materials reported in this study and in the literature (PDF)

AUTHOR INFORMATION

Corresponding Author

Juan Herranz − *Electrochemistry Laboratory, Paul Scherrer Institut, 5232 Villigen PSI, Switzerland;* ⬤ orcid.org/0000-0002-5805-6192; Email: juan.herranz@psi.ch

Authors

Piyush Chauhan − *Electrochemistry Laboratory, Paul Scherrer Institut, 5232 Villigen PSI, Switzerland;* ⬤ orcid.org/0000-0002-2155-6193

Karl Hiekel − *Physical Chemistry, Technische Universität Dresden, 01062 Dresden, Germany*

Justus S. Diercks − *Electrochemistry Laboratory, Paul Scherrer Institut, 5232 Villigen PSI, Switzerland*

Viktoriia A. Saveleva − *Electrochemistry Laboratory, Paul Scherrer Institut, 5232 Villigen PSI, Switzerland;* Present Address: European Synchrotron Radiation Facility, Grenoble, France (V.A.S.)

Pavel Khavlyuk − *Physical Chemistry, Technische Universität Dresden, 01062 Dresden, Germany*

Alexander Eychmüller − *Physical Chemistry, Technische Universität Dresden, 01062 Dresden, Germany*

Thomas J. Schmidt − *Electrochemistry Laboratory, Paul Scherrer Institut, 5232 Villigen PSI, Switzerland; Laboratory of Physical Chemistry, ETH Zürich, 8093 Zürich, Switzerland;* ⬤ orcid.org/0000-0002-1636-367X

Complete contact information is available at:
https://pubs.acs.org/10.1021/acsmaterialsau.1c00067

Notes

The authors declare no competing financial interest.

REFERENCES

(1) De Luna, P.; Hahn, C.; Higgins, D.; Jaffer, S. A.; Jaramillo, T. F.; Sargent, E. H. What Would It Take for Renewably Powered Electrosynthesis to Displace Petrochemical Processes? *Science* **2019**, *364*, No. eaav3506.

(2) Spurgeon, J. M.; Kumar, B. A Comparative Technoeconomic Analysis of Pathways for Commercial Electrochemical CO_2 Reduction to Liquid Products. *Energy Environ. Sci.* **2018**, *11*, 1536−1551.

(3) Jouny, M.; Luc, W.; Jiao, F. General Techno-Economic Analysis of CO_2 Electrolysis Systems. *Ind. Eng. Chem. Res.* **2018**, *57*, 2165−2177.

(4) Smith, W. A.; Burdyny, T.; Vermaas, D. A.; Geerlings, H. Pathways to Industrial-Scale Fuel out of Thin Air from CO_2 Electrolysis. *Joule* **2019**, *3*, 1822−1834.

(5) Kibria, M. G.; Edwards, J. P.; Gabardo, C. M.; Dinh, C.-T.; Seifitokaldani, A.; Sinton, D.; Sargent, E. H. Electrochemical CO_2 Reduction into Chemical Feedstocks: From Mechanistic Electrocatalysis Models to System Design. *Adv. Mater.* **2019**, *31*, No. 1807166.

(6) Durst, J.; Rudnev, A.; Dutta, A.; Fu, Y.; Herranz, J.; Kaliginedi, V.; Kuzume, A.; Permyakova, A. A.; Paratcha, Y.; Broekmann, P.;

Schmidt, T. J. Electrochemical CO_2 Reduction—a Critical View on Fundamentals, Materials and Applications. *CHIMIA Int. J. Chem.* **2015**, *69*, 769−776.

(7) Back, S.; Yeom, M. S.; Jung, Y. Understanding the Effects of Au Morphology on CO_2 Electrocatalysis. *J. Phys. Chem. C Nanomater. Interfaces* **2018**, *122*, 4274−4280.

(8) Kim, D.; Resasco, J.; Yu, Y.; Asiri, A. M.; Yang, P. Synergistic Geometric and Electronic Effects for Electrochemical Reduction of Carbon Dioxide Using Gold-Copper Bimetallic Nanoparticles. *Nat. Commun.* **2014**, *5*, 4948.

(9) Hori, Y.; Murata, A.; Kikuchi, K.; Suzuki, S. Electrochemical Reduction of Carbon Dioxides to Carbon Monoxide at a Gold Electrode in Aqueous Potassium Hydrogen Carbonate. *J. Chem. Soc., Chem. Commun.* **1987**, *10*, 728.

(10) Cave, E. R.; Montoya, J. H.; Kuhl, K. P.; Abram, D. N.; Hatsukade, T.; Shi, C.; Hahn, C.; Nørskov, J. K.; Jaramillo, T. F. Electrochemical CO_2 Reduction on Au Surfaces: Mechanistic Aspects Regarding the Formation of Major and Minor Products. *Phys. Chem. Chem. Phys.* **2017**, *19*, 15856−15863.

(11) Mezzavilla, S.; Horch, S.; Stephens, I. E. L.; Seger, B.; Chorkendorff, I. Structure Sensitivity in the Electrocatalytic Reduction of CO_2 with Gold Catalysts. *Angew. Chem. Int. Ed.* **2019**, *58*, 3774−3778.

(12) Dunwell, M.; Lu, Q.; Heyes, J. M.; Rosen, J.; Chen, J. G.; Yan, Y.; Jiao, F.; Xu, B. The Central Role of Bicarbonate in the Electrochemical Reduction of Carbon Dioxide on Gold. *J. Am. Chem. Soc.* **2017**, *139*, 3774−3783.

(13) Noda, H.; Ikeda, S.; Yamamoto, A.; Einaga, H.; Ito, K. Kinetics of Electrochemical Reduction of Carbon Dioxide on a Gold Electrode in Phosphate Buffer Solutions. *Bull. Chem. Soc. Jpn.* **1995**, *68*, 1889−1895.

(14) Mistry, H.; Reske, R.; Zeng, Z.; Zhao, Z.-J.; Greeley, J.; Strasser, P.; Cuenya, B. R. Exceptional Size-Dependent Activity Enhancement in the Electroreduction of CO_2 over Au Nanoparticles. *J. Am. Chem. Soc.* **2014**, *136*, 16473−16476.

(15) Mascaretti, L.; Niorettini, A.; Bricchi, B. R.; Ghidelli, M.; Naldoni, A.; Caramori, S.; Li Bassi, A.; Berardi, S. Syngas Evolution from CO_2 Electroreduction by Porous Au Nanostructures. *ACS Appl. Energy Mater.* **2020**, *3*, 4658−4668.

(16) Lu, X.; Yu, T.; Wang, H.; Qian, L.; Lei, P. Electrochemical Fabrication and Reactivation of Nanoporous Gold with Abundant Surface Steps for CO_2 Reduction. *ACS Catal.* **2020**, *10*, 8860−8869.

(17) Chen, Y.; Li, C. W.; Kanan, M. W. Aqueous CO_2 Reduction at Very Low Overpotential on Oxide-Derived Au Nanoparticles. *J. Am. Chem. Soc.* **2012**, *134*, 19969−19972.

(18) Kim, J.; Song, J. T.; Ryoo, H.; Kim, J. G.; Chung, S. Y.; Oh, J. Morphology-Controlled Au Nanostructures for Efficient and Selective Electrochemical CO_2 Reduction. *J. Mater. Chem. A* **2018**, *6*, 5119−5128.

(19) Zhao, S.; Jin, R.; Jin, R. Opportunities and Challenges in CO_2 Reduction by Gold-and Silver-Based Electrocatalysts: From Bulk Metals to Nanoparticles and Atomically Precise Nanoclusters. *ACS Energy Lett.* **2018**, *3*, 452−462.

(20) Kinoshita, K. Particle Size Effects for Oxygen Reduction on Highly Dispersed Platinum in Acid Electrolytes. *J. Electrochem. Soc.* **1990**, *137*, 845−848.

(21) Gasteiger, H. A.; Kocha, S. S.; Sompalli, B.; Wagner, F. T. Activity Benchmarks and Requirements for Pt, Pt-Alloy, and Non-Pt Oxygen Reduction Catalysts for PEMFCs. *Appl. Catal. B* **2005**, *56*, 9−35.

(22) Mayrhofer, K. J. J.; Blizanac, B. B.; Arenz, M.; Stamenkovic, V. R.; Ross, P. N.; Markovic, N. M. The Impact of Geometric and Surface Electronic Properties of Pt-Catalysts on the Particle Size Effect in Electrocatalysis. *J. Phys. Chem. B* **2005**, *109*, 14433−14440.

(23) Durst, J.; Simon, C.; Siebel, A.; Rheinländer, P. J.; Schuler, T.; Hanzlik, M.; Herranz, J.; Hasché, F.; Gasteiger, H. A. (Invited) Hydrogen Oxidation and Evolution Reaction (HOR/HER) on Pt Electrodes in Acid vs. Alkaline Electrolytes: Mechanism, Activity and Particle Size Effects. *ECS Trans.* **2014**, *64*, 1069−1080.

(24) Herranz, J.; Durst, J.; Fabbri, E.; Patru, A.; Cheng, X.; Permyakova, A. A.; Schmidt, T. J. Interfacial Effects on the Catalysis of the Hydrogen Evolution, Oxygen Evolution and CO_2-Reduction Reactions for (Co-) Electrolyzer Development. *Nano Energy* **2016**, *29*, 4−28.

(25) Meini, S.; Piana, M.; Beyer, H.; Schwämmlein, J.; Gasteiger, H. A. Effect of Carbon Surface Area on First Discharge Capacity of Li-O_2 Cathodes and Cycle-Life Behavior in Ether-Based Electrolytes. *J. Electrochem. Soc.* **2012**, *159*, A2135.

(26) Lu, Y.-C.; Gasteiger, H. A.; Shao-Horn, Y. Catalytic Activity Trends of Oxygen Reduction Reaction for Nonaqueous Li-Air Batteries. *J. Am. Chem. Soc.* **2011**, *133*, 19048−19051.

(27) Wei, C.; Sun, S.; Mandler, D.; Wang, X.; Qiao, S. Z.; Xu, Z. J. Approaches for Measuring the Surface Areas of Metal Oxide Electrocatalysts for Determining Their Intrinsic Electrocatalytic Activity. *Chem. Soc. Rev.* **2019**, *48*, 2518−2534.

(28) Morales, D. M.; Risch, M. Seven Steps to Reliable Cyclic Voltammetry Measurements for the Determination of Double Layer Capacitance. *J. Phys. Energy* **2021**, *3*, No. 034013.

(29) Trasatti, S.; Petrii, O. A. Real Surface Area Measurements in Electrochemistry. *Pure Appl. Chem.* **1991**, *63*, 711−734.

(30) Markovic, N. M.; Gasteiger, H. A.; Ross, P. N. J. Copper Electrodeposition on Pt (111) in the Presence of Chloride and (Bi) Sulfate: Rotating Ring-Pt (111) Disk Electrode Studies. *Langmuir* **1995**, *11*, 4098−4108.

(31) Santos, M. C.; Mascaro, L. H.; Machado, S. A. S. Voltammetric and Rotating Ring-Disk Studies of Underpotential Deposition of Ag and Cu on Polycrystalline Au Electrodes in Aqueous H_2SO_4. *Electrochim. Acta* **1998**, *43*, 2263−2272.

(32) Herrero, E.; Buller, L. J.; Abruña, H. D. Underpotential Deposition at Single Crystal Surfaces of Au, Pt, Ag and Other Materials. *Chem. Rev.* **2001**, *101*, 1897−1930.

(33) Baturina, O. A.; Lu, Q.; Padilla, M. A.; Xin, L.; Li, W.; Serov, A.; Artyushkova, K.; Atanassov, P.; Xu, F.; Epshteyn, A.; Brintlinger, T.; Schuette, M.; Collins, G. E. CO_2 Electroreduction to Hydrocarbons on Carbon-Supported Cu Nanoparticles. *ACS Catal.* **2014**, *4*, 3682−3695.

(34) Zhu, W.; Michalsky, R.; Metin, Ö.; Lv, H.; Guo, S.; Wright, C. J.; Sun, X.; Peterson, A. A.; Sun, S. Monodisperse Au Nanoparticles for Selective Electrocatalytic Reduction of CO_2 to CO. *J. Am. Chem. Soc.* **2013**, *135*, 16833−16836.

(35) Zhu, W.; Zhang, Y.-J.; Zhang, H.; Lv, H.; Li, Q.; Michalsky, R.; Peterson, A. A.; Sun, S. Active and Selective Conversion of CO_2 to CO on Ultrathin Au Nanowires. *J. Am. Chem. Soc.* **2014**, *136*, 16132−16135.

(36) Salih, T.; Brown, S. M.; Kim, C.; Carroll, K. J.; Brushett, F. R.; Bumajdad, A. Cost Effective and Scalable Synthesis of Supported Au Nanoparticles for the Electroreduction of CO_2 to CO. *Sci. Adv. Mater.* **2017**, *9*, 888−895.

(37) Cai, B.; Wen, D.; Liu, W.; Herrmann, A.-K.; Benad, A.; Eychmüller, A. Function-Led Design of Aerogels: Self-Assembly of Alloyed PdNi Hollow Nanospheres for Efficient Electrocatalysis. *Angew. Chem. Int. Ed.* **2015**, *54*, 13101−13105.

(38) Cai, B.; Eychmüller, A. Promoting Electrocatalysis upon Aerogels. *Adv. Mater.* **2019**, *31*, No. e1804881.

(39) Henning, S.; Ishikawa, H.; Kühn, L.; Herranz, J.; Müller, E.; Eychmüller, A.; Schmidt, T. J. Unsupported Pt-Ni Aerogels with Enhanced High Current Performance and Durability in Fuel Cell Cathodes. *Angew. Chem. Int. Ed.* **2017**, *56*, 10707−10710.

(40) Henning, S.; Shimizu, R.; Herranz, J.; Kühn, L.; Eychmüller, A.; Uchida, M.; Kakinuma, K.; Schmidt, T. J. Unsupported Pt_3Ni Aerogels as Corrosion Resistant PEFC Anode Catalysts under Gross Fuel Starvation Conditions. *J. Electrochem. Soc.* **2018**, *165*, F3001−F3006.

(41) Henning, S.; Herranz, J.; Ishikawa, H.; Kim, B. J.; Abbott, D.; Kühn, L.; Eychmüller, A.; Schmidt, T. J. Durability of Unsupported Pt-Ni Aerogels in PEFC Cathodes. *J. Electrochem. Soc.* **2017**, *164*, F1136−F1141.

(42) Shi, Q.; Zhu, C.; Zhong, H.; Su, D.; Li, N.; Engelhard, M. H.; Xia, H.; Zhang, Q.; Feng, S.; Beckman, S. P.; du, D.; Lin, Y. Nanovoid Incorporated Ir x Cu Metallic Aerogels for Oxygen Evolution Reaction Catalysis. *ACS Energy Lett.* **2018**, *3*, 2038−2044.

(43) Liu, W.; Rodriguez, P.; Borchardt, L.; Foelske, A.; Yuan, J.; Herrmann, A.-K.; Geiger, D.; Zheng, Z.; Kaskel, S.; Gaponik, N.; Kötz, R.; Schmidt, T. J.; Eychmüller, A. Bimetallic Aerogels: High-Performance Electrocatalysts for the Oxygen Reduction Reaction. *Angew. Chem. Int. Ed.* **2013**, *52*, 9849−9852.

(44) Fan, X.; Zerebecki, S.; Du, R.; Hübner, R.; Marzum, G.; Jiang, G.; Hu, Y.; Barcikowski, S.; Reichenberger, S.; Eychmüller, A. Promoting the Electrocatalytic Performance of Noble Metal Aerogels by Ligand-Directed Modulation. *Angew. Chem. Int. Ed.* **2020**, *59*, 5706−5711.

(45) Du, R.; Jin, W.; Wu, H.; Hübner, R.; Zhou, L.; Xue, G.; Hu, Y.; Eychmüller, A. Rapid Synthesis of Gold−Palladium Core−Shell Aerogels for Selective and Robust Electrochemical CO$_2$ Reduction. *J. Mater. Chem. A Mater. Energy Sustain.* **2021**, *9*, 17189−17197.

(46) Diercks, J. S.; Pribyl-Kranewitter, B.; Herranz, J.; Chauhan, P.; Faisnel, A.; Schmidt, T. J. An Online Gas Chromatography Cell Setup for Accurate CO$_2$-Electroreduction Product Quantification. *J. Electrochem. Soc.* **2021**, *168*, No. 064504.

(47) Hiekel, K.; Jungblut, S.; Georgi, M.; Eychmüller, A. Tailoring the Morphology and Fractal Dimension of 2D Mesh-like Gold Gels. *Angew. Chem. Int. Ed.* **2020**, *59*, 12048−12054.

(48) Tremiliosi-Filho, G.; Dall'Antonia, L. H.; Jerkiewicz, G. Limit to Extent of Formation of the Quasi-Two-Dimensional Oxide State on Au Electrodes. *J. Electroanal. Chem.* **1997**, *422*, 149−159.

(49) Goyal, A.; Marcandalli, G.; Mints, V. A.; Koper, M. T. M. Competition between CO$_2$ Reduction and Hydrogen Evolution on a Gold Electrode under Well-Defined Mass Transport Conditions. *J. Am. Chem. Soc.* **2020**, *142*, 4154−4161.

(50) Henning, S.; Herranz, J.; Gasteiger, H. A. Bulk-Palladium and Palladium-on-Gold Electrocatalysts for the Oxidation of Hydrogen in Alkaline Electrolyte. *J. Electrochem. Soc.* **2015**, *162*, F178−F189.

(51) Schlögl, K.; Mayrhofer, K. J. J.; Hanzlik, M.; Arenz, M. Identical-Location TEM Investigations of Pt/C Electrocatalyst Degradation at Elevated Temperatures. *J. Electroanal. Chem.* **2011**, *662*, 355−360.

(52) Kedzierzawski, P.; Augustynski, J. Poisoning and Activation of the Gold Cathode during Electroreduction of CO$_2$. *J. Electrochem. Soc.* **1994**, *141*, L58−L60.

(53) Łukaszewski, M.; Soszko, M.; Czerwiński, A. Electrochemical Methods of Real Surface Area Determination of Noble Metal Electrodes−an Overview. *Int. J. Electrochem. Sci.* **2016**, *11*, 4442−4469.

(54) Burke, L. D.; Nugent, P. F. The Electrochemistry of Gold: I the Redox Behaviour of the Metal in Aqueous Media. *Gold Bull.* **1997**, *30*, 43−53.

(55) Lertanantawong, B.; O'Mullane, A. P.; Surareungchai, W.; Somasundrum, M.; Burke, L. D.; Bond, A. M. Study of the Underlying Electrochemistry of Polycrystalline Gold Electrodes in Aqueous Solution and Electrocatalysis by Large Amplitude Fourier Transformed Alternating Current Voltammetry. *Langmuir* **2008**, *24*, 2856−2868.

(56) Vesztergom, S.; Ujvári, M.; Láng, G. G. RRDE Experiments with Potential Scans at the Ring and Disk Electrodes. *Electrochem. Commun.* **2011**, *13*, 378−381.

(57) Rheinländer, P. J.; Herranz, J.; Durst, J.; Gasteiger, H. A. Kinetics of the Hydrogen Oxidation/Evolution Reaction on Polycrystalline Platinum in Alkaline Electrolyte Reaction Order with Respect to Hydrogen Pressure. *J. Electrochem. Soc.* **2014**, *161*, F1448−F1457.

(58) Shinozaki, K.; Zack, J. W.; Pylypenko, S.; Pivovar, B. S.; Kocha, S. S. Oxygen Reduction Reaction Measurements on Platinum Electrocatalysts Utilizing Rotating Disk Electrode Technique: II. Influence of Ink Formulation, Catalyst Layer Uniformity and Thickness. *J. Electrochem. Soc.* **2015**, *162*, F1384.

(59) Ferreira, P. J.; Shao-Horn, Y.; Morgan, D.; Makharia, R.; Kocha, S.; Gasteiger, H. A. Instability of Pt/C Electrocatalysts in Proton Exchange Membrane Fuel Cells: A Mechanistic Investigation. *J. Electrochem. Soc.* **2005**, *152*, 2256.

(60) Nash, J.; Yang, X.; Anibal, J.; Wang, J.; Yan, Y.; Xu, B. Electrochemical Nitrogen Reduction Reaction on Noble Metal Catalysts in Proton and Hydroxide Exchange Membrane Electrolyzers. *J. Electrochem. Soc.* **2017**, *164*, F1712−F1716.

(61) Povia, M.; Herranz, J.; Binninger, T.; Nachtegaal, M.; Diaz, A.; Kohlbrecher, J.; Abbott, D. F.; Kim, B.-J.; Schmidt, T. J. Combining SAXS and XAS to Study the Operando Degradation of Carbon-Supported Pt-Nanoparticle Fuel Cell Catalysts. *ACS Catal.* **2018**, *8*, 7000−7015.

(62) Durst, J.; Simon, C.; Hasché, F.; Gasteiger, H. A. Hydrogen Oxidation and Evolution Reaction Kinetics on Carbon Supported Pt, Ir, Rh, and Pd Electrocatalysts in Acidic Media. *J. Electrochem. Soc.* **2015**, *162*, F190−F203.

(63) Henning, S.; Kühn, L.; Herranz, J.; Durst, J.; Binninger, T.; Nachtegaal, M.; Werheid, M.; Liu, W.; Adam, M.; Kaskel, S.; Eychmüller, A.; Schmidt, T. J. Pt-Ni Aerogels as Unsupported Electrocatalysts for the Oxygen Reduction Reaction. *J. Electrochem. Soc.* **2016**, *163*, F998−F1003.

(64) Henning, S.; Kühn, L.; Herranz, J.; Nachtegaal, M.; Hübner, R.; Werheid, M.; Eychmüller, A.; Schmidt, T. J. Effect of Acid Washing on the Oxygen Reduction Reaction Activity of Pt-Cu Aerogel Catalysts. *Electrochim. Acta* **2017**, *233*, 210−217.

(65) Trevor, D. J.; Chidsey, C. E.; Loiacono, D. N. In Situ Scanning-Tunneling-Microscope Observation of Roughening, Annealing, and Dissolution of Gold (111) in an Electrochemical Cell. *Phys. Rev. Lett.* **1989**, *62*, 929−932.

(66) Smiljanić, M.; Petek, U.; Bele, M.; Ruiz-Zepeda, F.; Šala, M.; Jovanovič, P.; Gaberšček, M.; Hodnik, N. Electrochemical Stability and Degradation Mechanisms of Commercial Carbon-Supported Gold Nanoparticles in Acidic Media. *J. Phys. Chem. C Nanomater. Interfaces* **2021**, *125*, 635−647.

(67) Aldana-González, J.; Olvera-García, J.; Montes de Oca, M. G.; Romero-Romo, M.; Ramírez-Silva, M. T.; Palomar-Pardavé, M. Electrochemical Quantification of the Electro-Active Surface Area of Au Nanoparticles Supported onto an ITO Electrode by Means of Cu Upd. *Electrochem. Commun.* **2015**, *56*, 70−74.

(68) Cherevko, S.; Zeradjanin, A. R.; Topalov, A. A.; Kulyk, N.; Katsounaros, I.; Mayrhofer, K. J. J. Dissolution of Noble Metals during Oxygen Evolution in Acidic Media. *ChemCatChem* **2014**, *6*, 2219−2223.

(69) Yoshida, K.; Kuzume, A.; Broekmann, P.; Pobelov, I. V.; Wandlowski, T. Reconstruction and Electrochemical Oxidation of Au (110) Surface in 0. 1 M H2SO4. *Electrochim. Acta* **2014**, *139*, 281−288.

(70) Hung, C.-C.; Lim, P.-Y.; Chen, J.-R.; Shih, H. C. Corrosion of Carbon Support for PEM Fuel Cells by Electrochemical Quartz Crystal Microbalance. *J. Power Sources* **2011**, *196*, 140−146.

(71) Kasian, O.; Kulyk, N.; Mingers, A.; Zeradjanin, A. R.; Mayrhofer, K. J. J.; Cherevko, S. Electrochemical Dissolution of Gold in Presence of Chloride and Bromide Traces Studied by On-Line Electrochemical Inductively Coupled Plasma Mass Spectrometry. *Electrochim. Acta* **2016**, *222*, 1056−1063.

(72) Kuhl, K. P.; Hatsukade, T.; Cave, E. R.; Abram, D. N.; Kibsgaard, J.; Jaramillo, T. F. Electrocatalytic Conversion of Carbon Dioxide to Methane and Methanol on Transition Metal Surfaces. *J. Am. Chem. Soc.* **2014**, *136*, 14107−14113.

(73) Hori, Y.; Wakebe, H.; Tsukamoto, T.; Koga, O. Electrocatalytic Process of CO Selectivity in Electrochemical Reduction of CO$_2$ at Metal Electrodes in Aqueous Media. *Electrochim. Acta* **1994**, *39*, 1833−1839.

(74) Grosse, P.; Gao, D.; Scholten, F.; Sinev, I.; Mistry, H.; Roldan Cuenya, B. Dynamic Changes in the Structure, Chemical State and Catalytic Selectivity of Cu Nanocubes during CO$_2$ Electroreduction: Size and Support Effects. *Angew. Chem. Int. Ed.* **2018**, *57*, 6192−6197.

(75) Manthiram, K.; Surendranath, Y.; Alivisatos, A. P. Dendritic Assembly of Gold Nanoparticles during Fuel-Forming Electrocatalysis. *J. Am. Chem. Soc.* **2014**, *136*, 7237−7240.

(76) Trindell, J. A.; Clausmeyer, J.; Crooks, R. M. Size Stability and H2/CO Selectivity for Au Nanoparticles during Electrocatalytic CO_2 Reduction. *J. Am. Chem. Soc.* **2017**, *139*, 16161−16167.

(77) Rogers, C.; Perkins, W. S.; Veber, G.; Williams, T. E.; Cloke, R. R.; Fischer, F. R. Synergistic Enhancement of Electrocatalytic CO_2 Reduction with Gold Nanoparticles Embedded in Functional Graphene Nanoribbon Composite Electrodes. *J. Am. Chem. Soc.* **2017**, *139*, 4052−4061.

📖 **Recommended by ACS**

Bridge Sites of Au Surfaces Are Active for Electrocatalytic CO_2 Reduction

Zixu Tao, Hailiang Wang, *et al.*

MAY 04, 2022
JOURNAL OF THE AMERICAN CHEMICAL SOCIETY   READ ☑

Controlling the Size of Au Nanoparticles on Reducible Oxides with the Electrochemical Potential

Dongha Kim, Bilge Yildiz, *et al.*

NOVEMBER 28, 2022
JOURNAL OF THE AMERICAN CHEMICAL SOCIETY   READ ☑

Au^{3+} Species-Induced Interfacial Activation Enhances Metal–Support Interactions for Boosting Electrocatalytic CO_2 Reduction to CO

Xiao-Chen Sun, Ya-Wen Zhang, *et al.*

DECEMBER 30, 2021
ACS CATALYSIS   READ ☑

Wavelength-Dependent Selective Acceleration of CO_2 Reduction and H_2 Evolution Using a Plasmonic Gold Nanorod Electrode

Toshihiro Takashima, Hiroshi Irie, *et al.*

JULY 27, 2022
ACS APPLIED NANO MATERIALS   READ ☑

Get More Suggestions >